

## NON-BAROTROPIC LINEAR ROSSBY WAVE INSTABILITY IN THREE-DIMENSIONAL DISKS

MIN-KAI LIN

Canadian Institute for Theoretical Astrophysics, 60 St. George Street, Toronto, ON M5S 3H8, Canada; [mklin924@cita.utoronto.ca](mailto:mklin924@cita.utoronto.ca)  
Received 2012 September 3; accepted 2013 January 8; published 2013 February 20

### ABSTRACT

Astrophysical disks with localized radial structure, such as protoplanetary disks containing dead zones or gaps due to disk–planet interaction, may be subject to the non-axisymmetric Rossby wave instability (RWI) that leads to vortex formation. The linear instability has recently been demonstrated in three-dimensional (3D) barotropic disks. It is the purpose of this study to generalize the 3D linear problem to include an energy equation, thereby accounting for baroclinity in three dimensions. Linear stability calculations are presented for radially structured, vertically stratified, geometrically thin disks with non-uniform entropy distribution in both directions. Polytopic equilibria are considered but adiabatic perturbations assumed. The unperturbed disk has a localized radial density bump, making it susceptible to the RWI. The linearized fluid equations are solved numerically as a partial differential equation eigenvalue problem. Emphasis on the ease of method implementation is given. It is found that when the polytropic index is fixed and adiabatic index increased, non-uniform entropy has negligible effect on the RWI growth rate, but pressure and density perturbation magnitudes near a pressure enhancement increase away from the midplane. The associated meridional flow is also qualitatively changed from homentropic calculations. Meridional vortical motion is identified in the nonhomentropic linear solution, as well as in a nonlinear global hydrodynamic simulation of the RWI in an initially isothermal disk evolved adiabatically. Numerical results suggest that buoyancy forces play an important role in the internal flow of Rossby vortices.

*Key words:* accretion, accretion disks – hydrodynamics – instabilities – methods: analytical – methods: numerical – protoplanetary disks

*Online-only material:* color figures

### 1. INTRODUCTION

Understanding the stability and evolution of radially structured disks is important for several astrophysical applications. Protoplanetary disks are likely to have complex radial structure (Terquem 2008; Armitage 2011) such as the radial boundary between magnetically active and inactive regions of the disk (“dead zones;” Gammie 1996) and edges of gaps induced by a giant planet (Lin & Papaloizou 1986).

Local variations in the disk profile, which are involved in both of the above examples, are vulnerable to the so-called Rossby wave instability (RWI; Lovelace et al. 1999; Li et al. 2000, 2001). The RWI is a linear shear instability associated with an extremum in the potential vorticity profile of the disk, or a generalization thereof, and leads to local vortex formation in the nonlinear regime. This has been verified for both dead zone boundary and planetary gaps in two-dimensional (2D) disks (e.g., Varnière & Tagger 2006; Lyra et al. 2008, 2009; Li et al. 2009; Lin & Papaloizou 2011; Crespe et al. 2011).

Previous studies have shown that disk vortices are able to concentrate dust particles, potentially assisting planetesimal formation (Barge & Sommeria 1995; Inaba & Barge 2006), which is of course crucial for planet formation. They can also interact strongly with planets, leading to non-monotonic orbital migration (Yu et al. 2010; Lin & Papaloizou 2010). Although protoplanetary disks are thin, they are nevertheless three-dimensional (3D), so modeling these processes in 3D is necessary.

Recently, the RWI has been demonstrated in 3D geometry in the context of protoplanetary disks (Meheut et al. 2010, 2012a, 2012b, 2012c; Umurhan 2010; Lin 2012a, 2012b, 2013; Lyra & Mac Low 2012). These models have, however,

employed a barotropic or nearly barotropic equation of state. They can therefore be regarded as the thin-disk version of the Papaloizou–Pringle instability (PPI; Papaloizou & Pringle 1984, 1985, 1987; Goldreich et al. 1986; Narayan et al. 1987), originally discovered for 3D pressure-supported thick tori. It is clearly of interest to extend 3D RWI calculations to non-barotropic flow, which was one of the features that distinguished the 2D RWI from the original PPI (Lovelace et al. 1999).

Given that the RWI and PPI involve the same physics, that is, wave coupling across co-rotation (Goldreich et al. 1986; Umurhan 2010), it is worth pointing out that the PPI has in fact been generalized to nonhomentropic tori. Frank & Robertson (1988) found that entropy gradients did not significantly affect instability growth rates, while Kojima et al. (1989) concluded that non-uniformity in entropy has similar effects as compressibility. They also found that perturbations have weak vertical dependence, in agreement with analytical arguments for homentropic flow (Papaloizou & Pringle 1985; Goldreich et al. 1986).

In this work, we study what is essentially the nonhomentropic PPI in rotationally supported thin 3D disks, a geometry relevant to protoplanetary disks. This is equivalent to an extension of the 2D RWI studies of Lovelace et al. (1999) to 3D, and we will adopt such nomenclature.

We consider the problem in the linear regime. Although the role of the RWI in protoplanetary disks must be determined through nonlinear hydrodynamic simulations, linear calculations are nevertheless a useful way to study the instability at low computational cost. It is also important to have such calculations at hand for comparison with nonlinear simulations.

Linear disturbances in 3D disks are governed by complicated partial differential equations (PDEs; Kato 2001). Even with a

numerical approach, computing unstable modes is no simple task. One method is to evolve the linear equations as an initial value problem (Papaloizou & Pringle 1987; Frank & Robertson 1988) and measure growth rates from data. For special disk equilibria, one can convert the problem to a set of ordinary differential equations (Tanaka et al. 2002; Zhang & Lai 2006; Meheut et al. 2012c; Lin 2012a, hereafter L12), but the derivation of these can be tedious. Thus, our study is also motivated by the desire to reduce this complexity when a numerical method is sought.

We pursue a numerical solution to the 2D eigenvalue problem. This approach has been taken by Kojima (1986, 1989) using finite-difference and finite-element methods. Inspired by the aforementioned studies, we employ finite differences in the radial direction and a pseudo-spectral method to treat the vertical direction (Lin 2013). We formulate the linear problem with numerical implementation in mind, so that much of the algebra can be taken care of by the numerical scheme, should one choose to do so.

This paper is organized as follows. In Section 2 we list the governing equations and describe the polytropic disk equilibria under consideration. The linear problem is defined in Section 3 and the numerical method is stated in Section 4. Linear simulations are presented in Section 5 for disks with moderate values of the polytropic index. Disks with an isothermal background are considered in Section 6, where a nonlinear hydrodynamic simulation is also described. We summarize in Section 7 with a discussion of important caveats and possible extensions to this study.

## 2. DISK MODEL

We consider a non-self-gravitating, inviscid fluid disk orbiting a central star of mass  $M_*$  and adopt cylindrical coordinates  $(r, \phi, z)$  centered on the star. The system is governed by the Euler equations:

$$\frac{\partial \rho}{\partial t} + \nabla \cdot (\rho \mathbf{v}) = 0, \quad (1)$$

$$\frac{\partial \mathbf{v}}{\partial t} + \mathbf{v} \cdot \nabla \mathbf{v} = -\frac{1}{\rho} \nabla p - \nabla \Phi_*, \quad (2)$$

$$\frac{\partial}{\partial t} \ln s + \mathbf{v} \cdot \nabla \ln s = 0, \quad (3)$$

where  $\rho$  is the mass density,  $\mathbf{v}$  is the velocity field,  $p$  is the pressure, and we refer to  $s \equiv p/\rho^\gamma$  as the entropy, where the ratio of specific heats  $\gamma$  is assumed constant. In the momentum equation,  $\Phi_*$  is the gravitational potential of the central star. Equation (3) describes adiabatic evolution.

A direct consequence of Equations (1) and (2) is an equation for the vortensity  $\zeta \equiv \nabla \times \mathbf{v}/\rho$ ,

$$\frac{D\zeta}{Dt} = \zeta \cdot \nabla \mathbf{v} + \frac{1}{\rho^3} \nabla \rho \times \nabla p, \quad (4)$$

where  $D/Dt \equiv \partial_t + \mathbf{v} \cdot \nabla$  is the Lagrangian derivative. The second term on the right-hand side is the baroclinic vorticity source. It is absent in barotropic flow for which  $p = p(\rho)$ . In this work, we consider barotropic equilibria but generally non-barotropic disturbances, so the baroclinic term is effective in the perturbed state.

### 2.1. Polytropic Equilibrium

The unperturbed disk is steady, axisymmetric, and polytropic, that is,

$$p = K\rho^{1+1/n}, \quad (5)$$

where  $K$  is a constant and  $n$  is the polytropic index. We adopt the thin-disk approximation (L12), so the density field has the simple form  $\rho = \rho_0(r)(1-z^2/H^2)^n$ , where  $\rho_0(r)$  is the midplane density and  $H(r)$  is the disk thickness.  $\rho_0$  is specified indirectly by imposing a surface density profile  $\Sigma \propto r^{-\alpha} B(r)$ , where  $B(r)$  is a Gaussian bump at  $r = r_0$  with amplitude  $A > 1$  and width  $\Delta r$  (Li et al. 2000). The aspect ratio at  $r_0$  is parameterized as  $h \equiv H(r_0)/r_0$ .

The unperturbed velocity field is  $(v_r, v_\phi, v_z) = (0, r\Omega, 0)$  with  $\Omega = \Omega(r)$  for barotropic equilibria and is given via centrifugal balance with gravity and pressure. Note that for a thin, non-self-gravitating disk the angular velocity is nearly Keplerian,  $\Omega \simeq \Omega_k \equiv \sqrt{GM_*/r^3}$ , where  $G$  is the gravitational constant.

The above setup is the same as in L12, and equations defining the equilibrium are listed therein. The limit  $n \rightarrow \infty$  corresponds to isothermal equilibria, and is treated as a special case in Section 6.

Polytropic equilibria are adopted for simplicity and to allow direct comparison with L12, which considered homentropic flow where  $\Gamma \equiv 1 + 1/n = \gamma$ . Then, Equation (5) holds in the perturbed disk, replacing Equation (3). Setting  $\gamma \neq \Gamma$  gives a nonhomentropic disk.

Following Lovelace et al. (1999), it is convenient to define the following length scales:

$$L_p = \left( \frac{1}{\gamma} \frac{\partial \ln p}{\partial r} \right)^{-1}, \quad H_p = \left( \frac{1}{\gamma} \frac{\partial \ln p}{\partial z} \right)^{-1}, \quad (6)$$

$$L_s = \left( \frac{1}{\gamma} \frac{\partial \ln s}{\partial r} \right)^{-1}, \quad H_s = \left( \frac{1}{\gamma} \frac{\partial \ln s}{\partial z} \right)^{-1}. \quad (7)$$

These are, respectively, the pressure and entropy length scales in the radial and vertical directions, which depend on both  $r$  and  $z$ . Note that for polytropic equilibria, the entropy and pressure length scales only differ by a constant multiplicative factor.

### 2.2. Stability Criteria

We consider disk equilibria satisfying the Solberg–Hoiland criteria for stability against axisymmetric perturbations:

$$\kappa^2 + N_r^2 + N_z^2 > 0, \quad \kappa^2 N_z^2 > 0, \quad (8)$$

where  $\kappa^2 = r^{-3} d(r^4 \Omega^2)/dr$  is the square of the epicycle frequency and

$$N_r^2 = -\frac{c_s^2}{L_p L_s}, \quad N_z^2 = -\frac{c_s^2}{H_p H_s} \quad (9)$$

are the square of the radial and vertical buoyancy frequencies, respectively, and  $c_s = (\gamma p/\rho)^{1/2}$  is the adiabatic sound speed (Tassoul 2000). We also define  $N^2 \equiv N_r^2 + N_z^2$ .

Our disk models satisfy the Rayleigh criterion  $\kappa^2 > 0$ , which limits the surface density bump amplitude.<sup>1</sup> Then we

<sup>1</sup> This also means that, by rescaling the density field, we can always make the Toomre stability parameter  $Q_T \equiv \bar{c}_s \kappa / \pi G \Sigma \gg 1$ , where  $\bar{c}_s$  is a typical sound speed, to satisfy the assumption of a non-self-gravitating disk.

require  $N_z^2 > 0$ , or stability against vertical convection, so the disk should be sub-adiabatically stratified with  $\Gamma < \gamma$ . For rotationally supported thin disks,  $|N_r^2| \ll \kappa^2$  so the first Solberg–Hoiland condition is generally satisfied regardless of the equation of state (Li et al. 2000). Note that  $N_z^2$  increases with  $z$ , so we expect the disk to be more stable at larger heights.

### 2.3. Instability Criterion

In the original 2D RWI calculations, Lovelace et al. (1999) found that when there is an extremum in the generalized vortensity profile  $\eta(r)$ , where

$$\eta = \frac{\kappa^2}{2\Omega\Sigma} \times \left( \frac{\Pi}{\Sigma^{\gamma_2}} \right)^{-2/\gamma_2}, \quad (10)$$

the disk may be unstable to non-axisymmetric perturbations localized about the extremum. Here,  $\Pi \equiv \int_{-\infty}^{\infty} p dz$  is the vertically integrated pressure and  $\gamma_2$  is the adiabatic index in the 2D energy equation  $D(\Pi\Sigma^{-\gamma_2})/Dt = 0$ .

To use Equation (10) in characterizing 3D disks, we use results from Goldreich et al. (1986) to relate  $\gamma_2$  and  $\gamma$ . Goldreich et al. studied linear disturbances in homentropic slender tori with a polytropic equation of state (Equation (5)). Assuming vertical hydrostatic equilibrium, they showed that the vertically integrated system has an effective polytropic index of  $n_2 = n + 1/2$ . If  $\gamma_2 = 1 + 1/n_2$  then  $\gamma_2 = (3\gamma - 1)/(\gamma + 1)$ . This relation has been used by other authors (e.g., Li et al. 2000; Klahr 2004). The assumptions made by Goldreich et al. do not strictly apply to our case (nonhomentropic equilibria and non-zero vertical motions) but their result will suffice for diagnostic purposes.

The polytropic disk equilibria have  $\Pi \propto \rho_0^\Gamma H$  and  $\Sigma \propto \rho_0 H$ , so the above definition gives

$$\eta \propto \frac{\kappa^2}{2\Omega} \Sigma^{(1-2\Gamma/\gamma_2)} H^{2(\Gamma-1)/\gamma_2}.$$

For the adopted parameter values, a surface density bump corresponds to a local minimum in the generalized vortensity, so that  $d\eta/dr \simeq 0$  at  $r = r_0$ . This is also close to a local  $\min(\kappa^2)$ . These minima act to “trap” disturbances, leading to instability (Li et al. 2000).

## 3. LINEAR PROBLEM

We consider Eulerian perturbations to the above equilibrium in the form  $\text{Re}[\delta\rho(r, z) \exp i(m\phi + \sigma t)]$  and similarly for other fluid variables. Here,  $m$  is the azimuthal wavenumber taken to be a positive integer and  $\sigma = -\omega - i\nu$  is a complex frequency, where  $-\omega$  is the real mode frequency and  $\nu$  is the growth rate. The co-rotation radius  $r_c$  of a mode is such that  $m\Omega(r_c) - \omega = 0$ , and the RWI is characterized by  $r_c \simeq r_0$ . For clarity, hereafter we omit writing out the time and azimuthal dependence explicitly.

The goal is to obtain a PDE for the quantity  $W \equiv \delta\rho/\rho$ . An explicit form of this equation is given by Kojima et al. (1989), but our priority is the ease of solution implementation. By writing individual equations in standard form—a sum of coefficients multiplying differential operators—we can formulate the linear problem with convenient variables, then transform to the desired ones by redefining said coefficients. These transformations can be done in the numerical code.

We begin by writing down the linearized equations in terms of the intermediate variables  $\tilde{W} = \rho W$  and  $\tilde{Q} \equiv c_s^2 \delta\rho$ .

The momentum equations give

$$\rho\delta v_r = -\frac{i}{D} \left( \bar{\sigma} \frac{\partial \tilde{W}}{\partial r} + \frac{2m\Omega}{r} \tilde{W} \right) + \frac{i\bar{\sigma}}{L_p D} \tilde{Q}, \quad (11)$$

$$\rho\delta v_\phi = \frac{1}{D} \left( \frac{\kappa^2}{2\Omega} \frac{\partial \tilde{W}}{\partial r} + \frac{m\bar{\sigma}}{r} \tilde{W} \right) - \frac{\kappa^2}{2\Omega L_p D} \tilde{Q}, \quad (12)$$

$$\rho\delta v_z = \frac{i}{\bar{\sigma}} \left( \frac{\partial \tilde{W}}{\partial z} - \frac{\tilde{Q}}{H_p} \right), \quad (13)$$

where  $\bar{\sigma} = \sigma + m\Omega$  is the shifted frequency and  $D = \kappa^2 - \bar{\sigma}^2$ . The linearized continuity equation is

$$i\bar{\sigma} \frac{\tilde{Q}}{c_s^2} + \frac{1}{r} \frac{\partial}{\partial r} (r\rho\delta v_r) + \frac{im}{r} \rho\delta v_\phi + \frac{\partial}{\partial z} (\rho\delta v_z) = 0, \quad (14)$$

and the linearized energy equation is

$$i\bar{\sigma}(\tilde{Q} - \tilde{W}) = c_s^2 \left[ \frac{1}{L_s} (\rho\delta v_r) + \frac{1}{H_s} (\rho\delta v_z) \right]. \quad (15)$$

Inserting the momentum equations into the continuity and energy equations yields a pair of PDEs:

$$\begin{aligned} \frac{\bar{\sigma}}{r} \frac{\partial}{\partial r} \left( \frac{r}{D} \frac{\partial \tilde{W}}{\partial r} \right) - \frac{1}{\bar{\sigma}} \frac{\partial^2 \tilde{W}}{\partial z^2} + \left[ \frac{2m}{r} \frac{\partial}{\partial r} \left( \frac{\Omega}{D} \right) - \frac{\bar{\sigma} m^2}{r^2 D} \right] \tilde{W} \\ - \frac{\bar{\sigma}}{r} \frac{\partial}{\partial r} \left( \frac{r\tilde{Q}}{L_p D} \right) + \frac{1}{\bar{\sigma}} \frac{\partial}{\partial z} \left( \frac{\tilde{Q}}{H_p} \right) + \left[ \frac{2m\Omega}{r L_p D} - \frac{\bar{\sigma}}{c_s^2} \right] \tilde{Q} = 0, \end{aligned} \quad (16)$$

$$\begin{aligned} \frac{\bar{\sigma}}{L_s D} \frac{\partial \tilde{W}}{\partial r} - \frac{1}{\bar{\sigma} H_s} \frac{\partial \tilde{W}}{\partial z} + \left[ \frac{2m\Omega}{r L_s D} - \frac{\bar{\sigma}}{c_s^2} \right] \tilde{W} \\ + \left[ \bar{\sigma} \left( \frac{1}{c_s^2} - \frac{1}{L_s L_p D} \right) + \frac{1}{\bar{\sigma} H_s H_p} \right] \tilde{Q} = 0. \end{aligned} \quad (17)$$

Equations (16) and (17) are the governing equations for linear disturbances.

Next, we transform to the coordinates  $(R, Z) = (r, z/H)$  so that the background disk structure is separable. For example, the density field becomes  $\rho = \rho_0(R)g(Z)$ . Then the unperturbed disk occupies a rectangular domain since  $g(\pm 1) = 0$ . The governing equations become

$$\begin{aligned} a_1 \frac{\partial^2 \tilde{W}}{\partial R^2} + b_1 \frac{\partial^2 \tilde{W}}{\partial Z \partial R} + c_1 \frac{\partial^2 \tilde{W}}{\partial Z^2} + d_1 \frac{\partial \tilde{W}}{\partial R} + e_1 \frac{\partial \tilde{W}}{\partial Z} + f_1 \tilde{W} \\ + \bar{d}_1 \frac{\partial \tilde{Q}}{\partial R} + \bar{e}_1 \frac{\partial \tilde{Q}}{\partial Z} + \bar{f}_1 \tilde{Q} = 0, \end{aligned} \quad (18)$$

$$d_2 \frac{\partial \tilde{W}}{\partial R} + e_2 \frac{\partial \tilde{W}}{\partial Z} + f_2 \tilde{W} + \bar{f}_2 \tilde{Q} = 0. \quad (19)$$

Explicit expressions for the coefficients are listed in Appendix A. We write the above PDE pair for  $(\tilde{W}, \tilde{Q})$  as

$$V_1 \tilde{W} + \bar{V}_1 \tilde{Q} = 0, \quad (20)$$

$$V_2 \tilde{W} + \tilde{V}_2 \tilde{Q} = 0. \quad (21)$$

Since  $\tilde{V}_2$  is a multiplicative factor, we can eliminate  $\tilde{Q}$  between Equations (20) and (21) to obtain an equation for  $\tilde{W}$ :

$$[V_1 - \tilde{V}_1 (\tilde{V}_2^{-1} V_2)] \tilde{W} \equiv V \tilde{W} = 0. \quad (22)$$

The operator  $V$  is obtained by updating the coefficients of  $V_1$ , so they have the same form. Finally, we substitute  $\tilde{W} = \rho W$  to obtain

$$UW = 0. \quad (23)$$

Construction of  $V$ , and hence  $U$ , requires the evaluation of  $\tilde{V}_1(\tilde{V}_2^{-1} V_2)$  which involves radial and vertical derivatives of the coefficients in Equation (19). In Appendix B we outline an alternative numerical approach which circumvents the algebra. (This appendix also includes relevant formulae to redefine the PDE coefficients for the transformation  $V \rightarrow U$ .)

The key dependent variable is  $W$ , but we also interpret results using  $Q \equiv \tilde{Q}/\rho$ . We refer to  $W$  and  $Q$  as pressure and density perturbations, respectively. Then the entropy perturbation is naturally defined as

$$S \equiv W - Q. \quad (24)$$

### 3.1. Boundary Conditions

We consider disturbances radially confined about the density bump at  $r = r_0$ , so the inner and outer disk boundaries play no significant role (Umurhan 2010). Hence, for simplicity we set  $\partial_R W = 0$  at radial boundaries.

Pressure and density perturbations are assumed to be symmetric about the disk midplane. Henceforth we consider  $z \geq 0$  without loss of generality. The default upper disk boundary condition is vanishing Lagrangian pressure perturbation at  $Z = Z_s$ :

$$\Delta p \equiv \delta p + \xi \cdot \nabla p = 0, \quad (25)$$

where  $\xi$  is the Lagrangian displacement ( $\nabla$  refers to cylindrical coordinates). We call this the free boundary condition. The surface function  $Z_s$  is assumed constant for simplicity. If  $Z_s$  is the zero-pressure surface, then Equation (25) can be satisfied automatically provided the perturbations are regular there. In practice, though, we take  $Z_s < 1$  to avoid the disk surface (where entropy and its derivatives diverge; Zhuravlev & Shakura 2007). Note that Equation (25), together with Equation (15), imply  $\Gamma Q = \gamma W$  at the upper boundary.

In some cases we adopt a solid upper boundary:

$$\delta v_z = Z_s \frac{dH}{dr} \delta v_r, \quad (26)$$

meaning no flow perpendicular to the boundary ( $\delta v_\perp = 0$ ), and occasionally we set  $\delta v_z = 0$ . Upper disk boundary conditions are imposed explicitly by replacing the governing equation with Equation (25) or (26) at  $Z = Z_s$ .

### 3.2. Baroclinity

Before proceeding to solve the linear equations, it is useful to have a qualitative picture of the solution to aid us in checking results. The main difference from L12 is baroclinity. Here,

we discuss expected effects of the baroclinic source term in Equation (4).

As we will often examine meridional flow, consider the azimuthal component of Equation (4), which can source vortical motion in the  $(r, z)$  plane. When linearized, this baroclinic source term becomes

$$\begin{aligned} \frac{1}{\rho^3} (\nabla \rho \times \nabla p)_\phi &\rightarrow \frac{1}{\rho^2} \left( \frac{1}{L_p} \frac{\partial}{\partial z} - \frac{1}{H_p} \frac{\partial}{\partial r} \right) \left( \tilde{Q} - \frac{\gamma}{\Gamma} \tilde{W} \right) \\ &= \frac{\Gamma}{\gamma \rho H} \left[ \underbrace{\frac{\rho'_0}{\rho_0} \frac{\partial \tilde{S}}{\partial Z}}_{\dagger} + \underbrace{\frac{2nZ}{(1-Z^2)} \frac{\partial \tilde{S}}{\partial R}}_{\ddagger} \right], \end{aligned} \quad (27)$$

where  $\tilde{S} \equiv Q - \gamma W/\Gamma$  and  $'$  denotes differentiation with respect to the argument. We have utilized the barotropic background in obtaining Equation (27). In the discussion below, perturbations are regarded as real quantities.

The RWI is characterized by non-axisymmetric pressure/density enhancements radially localized about the density bump (Li et al. 2001). Assuming this is qualitatively unchanged in a nonhomentropic disk, let us denote the midplane coordinate of the center of one such enhancement as  $(r_0, \phi_0)$ . We will precisely define  $\phi_0$  later. For now, consider the  $(r, z)$  plane at fixed  $\phi = \phi_0$  and about  $r = r_0$ .

Equation (27) shows that non-uniformity in  $\tilde{S}$  can cause vortical motion in the meridional plane. The distribution of  $\tilde{S}(R, Z)$  at the chosen azimuth can be anticipated as follows. Note that

$$\tilde{S} = \left(1 - \frac{\gamma}{\Gamma}\right) W - S.$$

We first deduce the sign of  $\tilde{S}(r_0, 0)$ . For a pressure enhancement,  $W(r_0, 0) > 0$  and  $(1 - \gamma/\Gamma)W(r_0, 0) < 0$  because  $\gamma > \Gamma$ . To determine the sign of the local entropy perturbation,  $S(r_0, 0)$ , we recall the background entropy  $s \propto \rho^{\Gamma-\gamma}$  so a density bump at  $r_0$  corresponds to an entropy dip there. Now, the RWI has caused a pressure/density enhancement at  $(r_0, 0)$ . This can be achieved by moving fluid in the vicinity of  $(r_0, 0)$ , which has higher entropy, toward  $(r_0, 0)$ . Then the midplane Eulerian entropy perturbation at  $r_0$  is positive, i.e.,  $S(r_0, 0) > 0$ . Therefore  $\tilde{S}(r_0, 0) < 0$ .

Next, the free boundary condition implies  $\tilde{S}(R, Z_s) = 0$ . So  $\tilde{S}(r_0, Z)$  varies from a negative value at the midplane to zero at the upper disk boundary. Then it is reasonable to assume  $\tilde{S}(r_0, Z) \leq 0$ . (A similar argument can be made for the solid upper boundary.) The perturbation magnitude  $|\tilde{S}|$  should also decrease radially away from  $r_0$  because the RWI presents radially localized disturbances.

A simple distribution to satisfy the above properties is for  $\tilde{S}$  to have a local minimum at  $(r_0, 0)$  and is negative or zero in this region. It is most negative at  $(r_0, 0)$  and becomes less negative away from it. Then  $\partial_Z \tilde{S} > 0$ , and  $\partial_R \tilde{S} \geq 0$  ( $\partial_R \tilde{S} \leq 0$ ) for  $R > r_0$  ( $R < r_0$ ).

Consider regions radially away from  $(r_0, 0)$ . From the argument above,  $\tilde{S}$  should be roughly 2D ( $\partial_Z \ll 1$ ) away from its minimum at  $(r_0, 0)$ . Then the sign of the baroclinic source (Equation (27)) is dictated by that of  $(\ddagger)$ . Even if  $\partial_Z = O(1)$  in these regions, we expect  $\partial_R \sim H^{-1}$  for a radially localized disturbance. Then the magnitude of  $(\dagger)$  relative to  $(\ddagger)$  is of order  $|H\rho'_0/Z\rho_0|(1-Z^2)$ , which is small for the adopted disk models (for  $Z \neq 0$ ). So away from  $r_0$  and the midplane, the radial variation of  $\tilde{S}$  is more important than its vertical variation. Of course, this argument does not apply where  $\partial_R \tilde{S} = 0$ , which occurs at  $Z = Z_s$  and is expected close to  $r = r_0$ .

Under the above assumptions we anticipate that away from the midplane but not very close to the upper disk boundary, the sign of the baroclinic source term is determined by the radial derivative of  $\bar{S}$ , which is positive (negative) exterior (interior) to  $r_0$ . Close to or at  $r_0$ , provided  $\bar{S}$  varies more rapidly in the vertical direction than radial, the sign of the baroclinic source is the same as that of  $\rho'_0$ , which is *typically* negative, but not always, due to a density bump.

#### 4. NUMERICAL PROCEDURE

The operator  $U$  can be written in the same form as  $V_1$ . A matrix representation of such an operator is described in Lin (2013) where details are given. We summarize here the main steps.

The radial coordinate is discretized into  $N_R$  uniformly spaced grid points. Let  $W_i(Z) \equiv W(R_i, Z)$  denote the solution along the vertical line  $R = R_i$ . We set

$$W_i(Z) = \sum_{k=1}^{N_Z} w_{ki} \psi_k(Z/Z_s), \quad (28)$$

where the basis functions  $\psi_k = T_{2(k-1)}$  are even Chebyshev polynomials of the first kind.  $N_Z$  is the number of basis functions and the highest polynomial order is  $l_{\max} = 2(N_Z - 1)$ .

Radial derivatives in  $UW$  are replaced by central finite differences, and we evaluate vertical derivatives exactly at the  $N_Z$  non-negative Lobatto grid points of  $T_{l_{\max}}(Z/Z_s)$ . This procedure performs the conversion

$$UW = 0 \rightarrow U\mathbf{w} = \mathbf{0}, \quad (29)$$

where  $U$  is a  $(N_R N_Z) \times (N_R N_Z)$  block tridiagonal matrix and  $\mathbf{w}$  is a vector storing the  $N_R N_Z$  pseudo-spectral coefficients  $w_{ki}$ .

The numerical problem is a set of linear homogeneous equations,  $U(\sigma)\mathbf{w} = \mathbf{0}$ . Non-trivial solutions exist if  $\det U = 0$ . This is achieved by varying  $\sigma$  using Newton–Raphson iteration. We only accept solutions where the reciprocal of the condition number of  $U$  is zero at machine precision. The same method of solution was employed in L12.

##### 4.1. Results Visualization

The pressure perturbation  $W$  is constructed from the pseudo-spectral coefficients  $w_{ki}$ . We then calculate  $Q$  from Equation (19) and velocity perturbations from Equations (11)–(13).

We examine real perturbations about the *vortex core*  $(r, \phi) = (r_0, \phi_0)$ , where  $m\phi_0 = -\arg[W(r_0, 0)]$ . Setting  $\phi = \phi_0$  is equivalent to redefining a physical perturbation as

$$X \rightarrow \text{Re}[X(r, z)W^*(r_0, 0)], \quad (30)$$

where  $X$  represents  $W$ ,  $Q$ ,  $S$ , or  $\delta\mathbf{v}$ , and  $*$  denotes complex conjugate. All perturbations are regarded as real hereafter. In practice  $(r_0, \phi_0)$  is close to a local maximum of pressure perturbation. The magnitude of  $X$ , as redefined above, is arbitrary but its sign is not.

As an empirical measure of flow three dimensionality, we compare vertical and horizontal motions near the bump radius using  $\langle \theta_m \rangle$ , where

$$\theta_m^2 = \frac{\delta v_z^2}{\delta v_r^2 + \delta v_\phi^2}, \quad (31)$$

and  $\langle \cdot \rangle$  denotes averaging over  $R \in [0.8, 1.2]r_0$  and  $Z \in [0, Z_s]$  at  $\phi = \phi_0$ .

**Table 1**  
Summary of Main Linear Simulations

Case	$\Gamma$	$\gamma$	BC <sup>a</sup>	$\omega/m\Omega_0$	$10^2\nu/\Omega_0$	$\langle \theta_m \rangle$
<i>h = 0.14</i>						
0	1.67	1.67	$\Delta p = 0$	0.9941	10.74	0.33
1	1.67	1.8	$\Delta p = 0$	0.9937	10.80	0.36
2	1.67	2.0	$\Delta p = 0$	0.9931	10.86	0.39
3a	1.67	2.5	$\Delta p = 0$	0.9919	10.99	0.44
3b	1.67	2.5	$\delta v_\perp = 0$	0.9911	11.34	0.41
4	1.67	3.0	$\Delta p = 0$	0.9910	11.07	0.47
<i>h = 0.2</i>						
5	1.4	1.4	$\Delta p = 0$	0.9923	16.66	0.24
6	1.33	1.4	$\Delta p = 0$	0.9917	13.81	0.31
7	1.29	1.4	$\Delta p = 0$	0.9912	11.38	0.34
8	1.25	1.4	$\Delta p = 0$	0.9909	9.246	0.36

**Note.** <sup>a</sup> Boundary condition at  $Z = Z_s$ .

#### 5. LINEAR SIMULATIONS

We adopt units such that  $G = M_* = 1$ . Our main calculations are summarized in Table 1. For these runs the computational domain is  $R \in [0.4, 1.6]r_0$ ,  $Z \in [0, Z_s] = [0, 0.9]$ , and  $\alpha = 0.5$  for the power-law part of the surface density profile. The bump radius, amplitude, and width are set to  $r_0 = 1$ ,  $A = 1.4$ , and  $\Delta r = 0.05r_0$ , respectively. We consider modes with  $m = 3$  unless otherwise stated. Slightly different setups are employed in Section 6 to explore the isothermal limit.

The new parameter for nonhomentropic disks, compared to homentropic flow in L12, is the adiabatic index  $\gamma$ . We therefore focus on examining the effect of entropy gradients due to  $\gamma \neq \Gamma$ . Cases 0–4 have fixed polytropic index  $n = 1.5$ , and therefore identical background density and velocity profiles, but variable adiabatic index  $\gamma \geq 5/3$ . Cases 5–8 have fixed adiabatic index  $\gamma = 1.4$ , but variable polytropic index  $n \geq 2.5$ .

An example of nonhomentropic equilibrium, with  $n = 1.5$  ( $\Gamma = 5/3$ ) and  $\gamma = 2.5$ , is shown in Figure 1 (case 3). The generalized vortensity and  $\kappa^2 + N^2$  are plotted. As expected for a density bump, the generalized vortensity has a local minimum at  $r = r_0$ . It corresponds to  $\min(\kappa^2/\Omega_k^2) = 0.43$ . The increase in  $\kappa^2 + N^2$  with respect to height is due to  $N_z^2$  (since  $N_r \sim hN_z$  near the upper boundary). Note that  $N_z^2 \gtrsim \Omega^2$  for  $|z| \gtrsim 0.7H$  in this case.

The discretized problem is solved with standard matrix routines provided in the LAPACK package. The default resolution is  $(N_R, N_Z) = (512, 12)$ , corresponding to  $l_{\max} = 22$ .

##### 5.1. Homentropic Reference Case

For comparison purposes, we reproduce the fiducial homentropic calculation in L12 by setting  $\gamma = 5/3$  (case 0). Then  $W = Q$  since  $L_s^{-1} = H_s^{-1} \equiv 0$  (Equation (15)). This also serves as a test for our numerical method. The eigenfrequency and perturbations shown in Table 1 and Figure 2 agrees well with L12. In co-rotation region  $R \in [0.8, 1.2]r_0$ ,  $W$  is nearly independent of height and the vortex core has upward motion.

##### 5.2. Nonhomentropic Example

We now examine case 3a with  $\gamma = 2.5$ ,  $\Gamma = 1.67$ . The eigenfrequency  $\sigma$  is close to case 0, but the growth rate is slightly larger in the nonhomentropic disk.

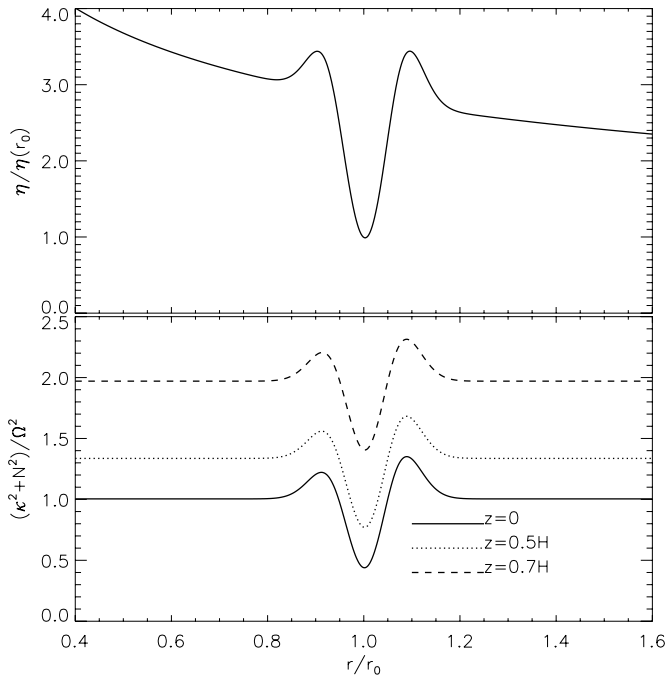


**Figure 1.** Equilibrium profile for a nonhomotropic disk with  $n = 1.5$  and  $\gamma = 2.5$  (case 3). The generalized vortensity (top) and  $\kappa^2 + N^2$  at three heights (bottom) are shown.

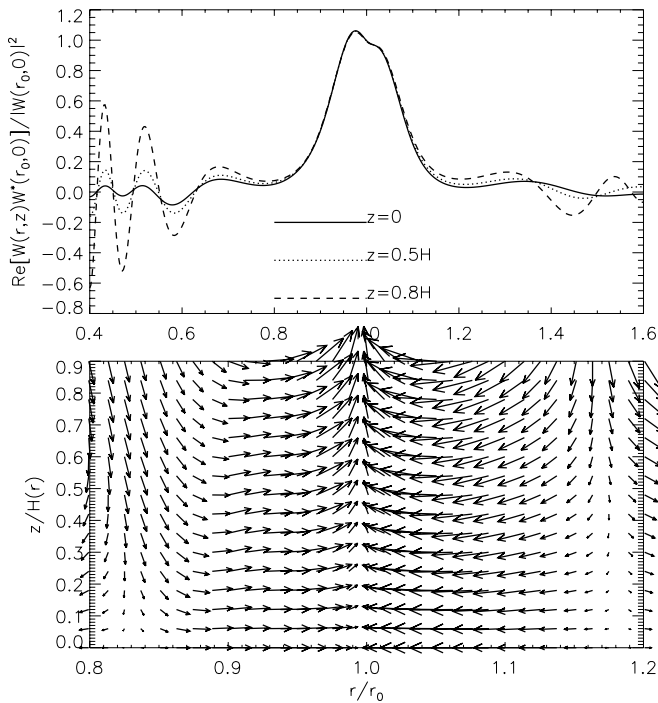


**Figure 2.** Real perturbations for the homotropic case 0 ( $\Gamma = \gamma = 1.67$ ). The pressure perturbation  $W$  at three heights (top) and meridional velocity perturbation (bottom) near the vortex core are shown.

Figure 3 shows the pressure, density, and entropy perturbations at several heights. Near  $r_0$ , pressure and density perturbations increase with height, unlike the homotropic case where  $W$  has weak  $z$  dependence. Nonhomotropic disks generally have  $W \neq Q$ , as shown in Figure 3. The difference between  $W$  and  $Q$  at the midplane is due to background radial entropy gradients  $L_s^{-1}$  since  $H_s^{-1}(r, 0) = 0$ .

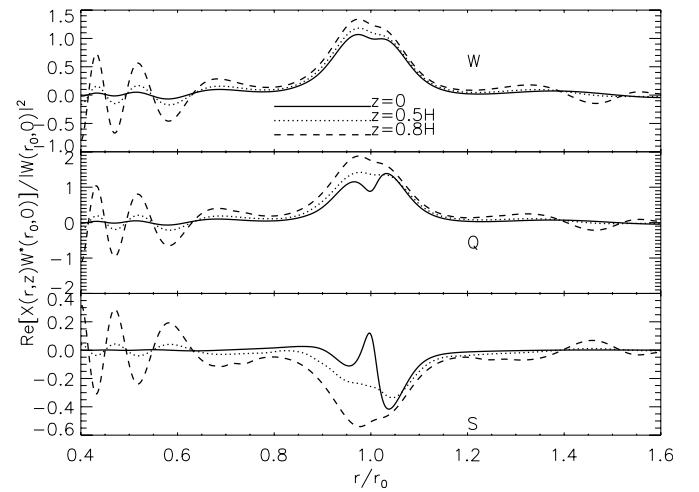


**Figure 3.** Pressure (top,  $W$ ), density (middle,  $Q$ ), and entropy (bottom,  $S$ ) perturbations for the nonhomotropic case 3a ( $\Gamma = 1.67$ ,  $\gamma = 2.5$ ).

At co-rotation, the density perturbation  $Q$  increases with height faster than the pressure perturbation  $W$ , which results in a negative entropy perturbation. This is consistent with the requirement  $S = (1 - \gamma/\Gamma)W$  at the upper disk boundary. It is clear that  $S$  has a stronger vertical dependence than either  $W$  or  $Q$ .

We might have expected the above result on physical grounds. The homotropic case indicates upward motion at the vortex core. If a positive (stable) vertical entropy gradient is introduced, then a fluid element displaced upward should increase its density compared to the surrounding background, i.e.,  $Q > 0$ , and this should become more positive with height because vertical velocities increase in magnitude with height. The pressure perturbation is not expected to change as rapidly because the fluid element can establish pressure equilibrium with its surroundings.

### 5.2.1. Entropy Perturbation

We plot the entropy perturbation  $S$  at  $z = 0$  and  $z = 0.8H$  in Figure 4. The figures are overlaid by the perturbed horizontal flow, which are similar at both heights. The anti-cyclonic flow pattern is commonly found in previous studies (e.g., Li et al. 2000, 2001). Entropy gradients of this magnitude do not affect this characteristic feature of the RWI.

Therefore, we could have inferred some of the features in Figure 4 without solving the fluid equations, by invoking entropy advection. Consider the linearized energy equation near co-rotation where  $\bar{\sigma} \simeq -i\nu$  (which is close to  $r_0$ ),

$$\delta s \sim -\nu^{-1} \delta v \cdot \nabla s, \quad (32)$$

and  $\nu > 0$  for a growing mode. Equation (32) is only valid within a small distance  $\epsilon \ll \nu/|m\Omega'_0|$  from  $r_0$ . In this example,  $\nu/|m\Omega'_0| \simeq 0.02r_0$ .

The midplane entropy has a dip at the bump radius but it increases globally in the radial direction, so  $\partial_r s > 0$  at  $r_0$ . This naturally implies that inward (outward) radial flow for  $\phi < \phi_0$  ( $\phi > \phi_0$ ), i.e., anti-cyclonic motion, brings about a local entropy increase (decrease) near  $r_0$  at  $z = 0$ . We recognize the qualitative similarity between the midplane flow pattern in Figure 4 and horseshoe turns induced by an embedded planet. Entropy advection then leads to large radial entropy gradients (Paardekooper et al. 2010), which can be seen in Figure 3 on

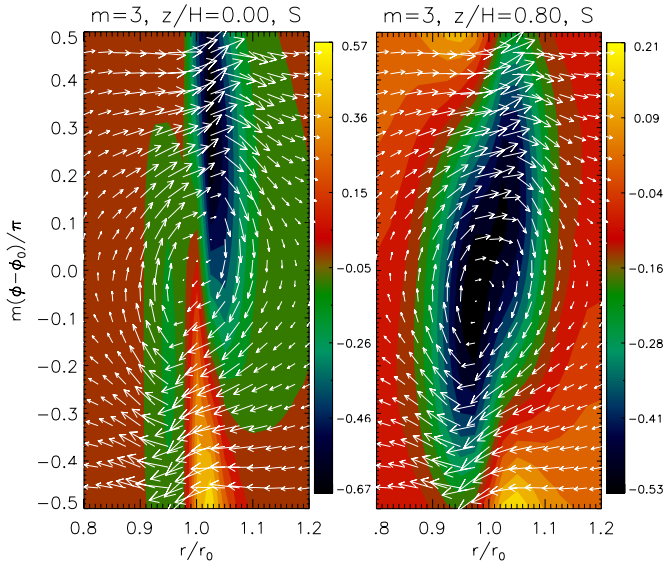


**Figure 4.** Entropy perturbation in midplane (left) and near the upper disk boundary (right) for the nonhomentropic case 3a. Arrows show the perturbed velocity field projected onto this plane.

(A color version of this figure is available in the online journal.)

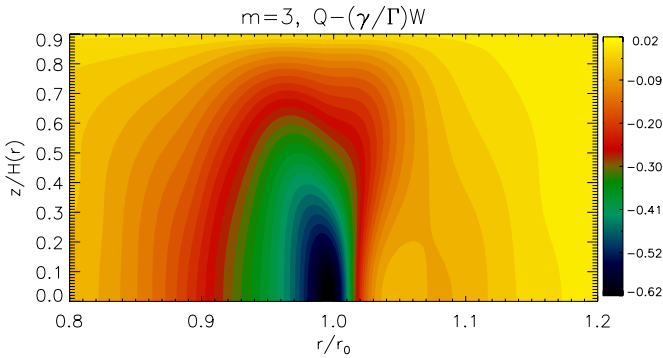


**Figure 5.** Map of the quantity  $\bar{S} \equiv Q - \gamma W / \Gamma$  for case 3a (the real perturbation at  $\phi = \phi_0$  is shown).  $\bar{S}$  appears in the baroclinic term in Equation (27), as well as the expression for vertical velocity in Equation (33). The local minimum near  $(r_0, 0)$  can be expected without solving the linear problem (see Section 3.2).

(A color version of this figure is available in the online journal.)

either side of  $r_0$  at the midplane. This gradient is, of course, growing exponentially in time, so it may be important even within the linear regime.

In the vertical dimension, if we assume the flow at  $(r_0, \phi_0)$  is unchanged from the homentropic case (i.e., upward), then since the background entropy increases with height, the local Eulerian entropy perturbation at the vortex core must become negative away from the midplane, as observed.

Related to the entropy perturbation is the quantity  $\bar{S} \equiv Q - \gamma W / \Gamma$ . Its distribution shown in Figure 5 agrees with expectations made in Section 3.2, namely it is mostly negative, with a local minimum at the vortex core.

### 5.2.2. Vertical Vorticity Perturbation

Figures 6 and 7 show the perturbation to vertical vorticity,  $\delta\omega_z \equiv \hat{z} \cdot \nabla \times \delta\mathbf{v}$ , in the horizontal and meridional planes, respectively. These plots agree with the identification of the linear RWI with a pair of edge waves propagating in the  $\pm\phi$  directions along radial potential vorticity gradients on either side of the bump radius  $r_0$  (Umurhan 2010).

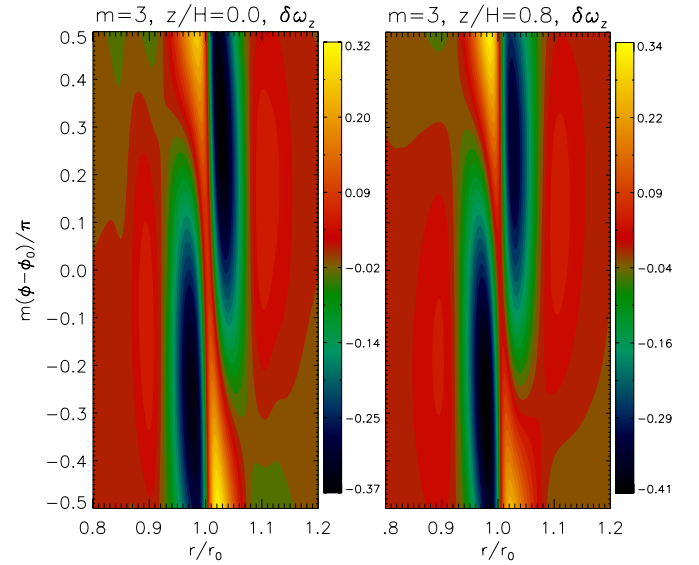


**Figure 6.** Perturbation to the vertical component of vorticity in the nonhomentropic case 3a at two heights in the horizontal plane. The vertical dependence is weak, but there is a slight increase in the maximum perturbation amplitude away from the midplane. This figure is qualitatively similar to the top panel of Figure 3 in Meheut et al. (2012a).

(A color version of this figure is available in the online journal.)

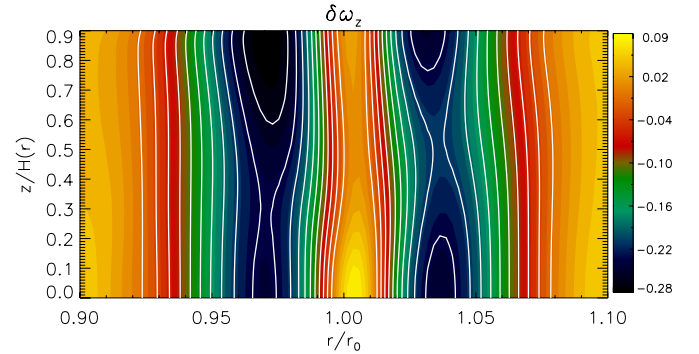


**Figure 7.** Perturbation to the vertical component of vorticity in the nonhomentropic case 3a, in the meridional plane at  $\phi = \phi_0$ . Regions of  $\delta\omega_z \leq 0$  are delineated by white lines.

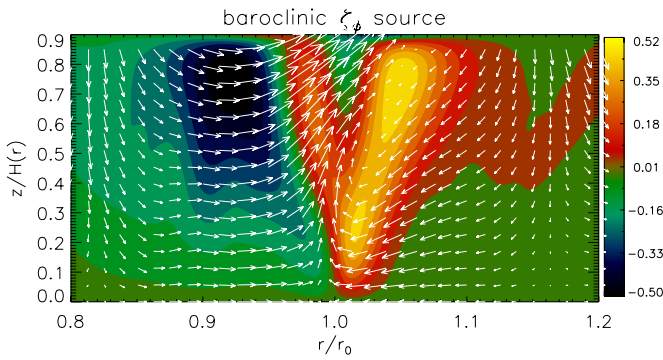
(A color version of this figure is available in the online journal.)

The background vorticity  $\omega_z$  has a dip at  $r_0$ . Then the positive/negative regions of  $\delta\omega_z$  in Figure 6 is broadly consistent with the advection of  $\omega_z$  by the perturbed horizontal flow, in a manner similar to the advection of entropy described in the previous section.

Although the perturbed flow in the nonhomentropic case consists of vorticity columns (Figure 7), there is actually a slight increase in  $\max(|\delta\omega_z|)$  away from the midplane. This contrasts to Umurhan’s analytical model of the RWI in polytropic disks, where horizontal velocities, and hence  $\delta\omega_z$ , have no vertical dependence.

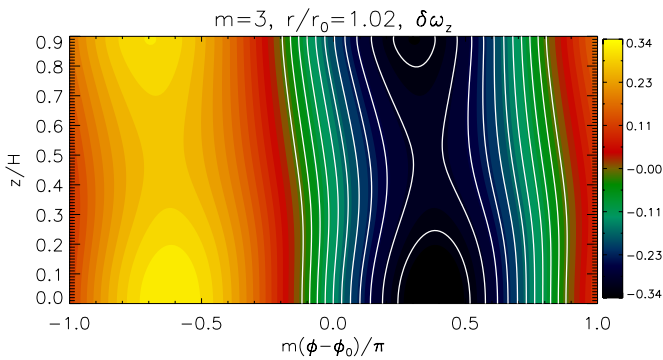
### 5.2.3. Meridional Vortical Flow and Tilted Vorticity Columns

Figure 8 shows the perturbed velocity field in the  $(r, z)$  plane, with a map of the baroclinic source term defined in Section 3.2. The flow pattern is similar to the homentropic case in that it is still converging toward  $r_0$ , and vertical motion is predominantly upward there. However, there is a notable difference from the homentropic case—vortical motion (of positive azimuthal vorticity) centered about  $(r, z) = (1.02r_0, 0.5H)$ . It coincides



**Figure 8.** Meridional flow in the nonhomentropic case 3a. The azimuth taken for this slice is  $\phi = \phi_0$ . The contours show the baroclinic source term for azimuthal vorticity (Equation (27) multiplied by  $\rho$ ). The arrows show the perturbed velocity field projected onto this plane.

(A color version of this figure is available in the online journal.)



**Figure 9.** Perturbation to vertical vorticity in the  $(\phi, z)$  plane at  $r = 1.02r_0$ . Regions of  $\delta\omega_z \leq 0$  are delineated by white lines. The center of the meridional vortical motion identified in Figure 8 occurs at  $(\phi, z) = (\phi_0, 0.5H)$ . The azimuthal range  $\phi - \phi_0 \in [-0.5, 0.5]\pi/m$  corresponds to anti-cyclonic motion about the vortex core.

(A color version of this figure is available in the online journal.)

with a region where the azimuthal baroclinic source term is positive. Note that the sign of the baroclinic source away from the midplane—being positive (negative) for  $r > r_0$  ( $r < r_0$ )—is roughly consistent with expectations made in Section 3.2.

Vortical motion in the meridional plane also correlates to misalignment between a column of negative vertical vorticity perturbation and the vertical direction. This is demonstrated in Figure 9 where contours of  $\delta\omega_z$  are shown to be tilted in the  $(\phi, z)$  plane. We can quantify this tilt by calculating  $1 - \langle \cos \theta \rangle_Z$ , where

$$\cos \theta \equiv |\partial_\phi \delta\omega_z| / [(\partial_Z \delta\omega_z)^2 + (\partial_\phi \delta\omega_z)^2]^{1/2}$$

and  $\langle \cdot \rangle_Z$  denotes averaging over the vertical direction at fixed  $\phi = \phi_0$  shown in Figure 9.

For the nonhomentropic case 3a, we find  $1 - \langle \cos \theta \rangle_Z = 0.011$ . This value should be compared with the homentropic case 0 where  $1 - \langle \cos \theta \rangle_Z = 3.4 \times 10^{-5}$  and the tilt is hardly noticeable.

We rationalize the small tilt observed in Figure 9 by interpreting the nonhomentropic solution as a small deviation from the homentropic case, for which the tilt is negligible and lines of constant  $\delta\omega_z < 0$  are parallel to the vertical axis. Now consider baroclinity as a perturbation to this configuration.

The discussion in Section 3.2, together with Figure 8, suggests that baroclinity gives rise to positive azimuthal vorticity (as evident from the meridional flow pattern). We can produce

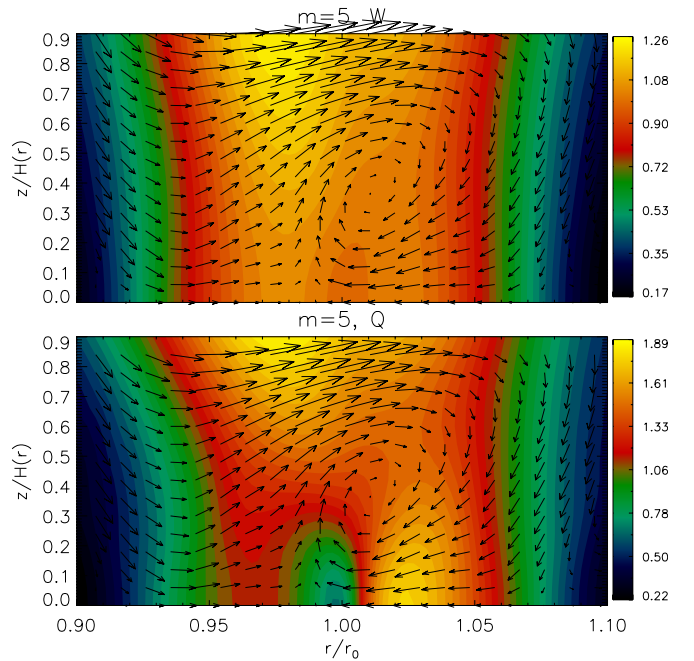


**Figure 10.** Pressure ( $W$ , top) and density ( $Q$ , bottom) perturbation for the  $m = 5$  mode in the nonhomentropic case 3a. The meridional flow is also shown.

(A color version of this figure is available in the online journal.)

azimuthal vorticity by tilting a vertical column negative of  $\delta\omega_z$  in the azimuthal direction indicated in Figure 9. By such a tilt, what was purely horizontal *local* anti-cyclonic motion, associated with  $\delta\omega_z < 0$  being a vertical column, now has a non-zero projection onto the meridional plane. This results in the meridional vortical motion demanded by the baroclinity in nonhomentropic flow. In other words, baroclinity has converted some of the horizontal motion of the homentropic flow into vertical motion.

#### 5.2.4. $m = 5$

The meridional flow varies with  $m$ . Figure 10 shows the  $m = 5$  solution for the setup of case 3a. We focus on the region  $R \in [0.9, 1.1]r_0$  because higher- $m$  modes are not as well localized as low- $m$  (Lin & Papaloizou 2011). It displays stronger vortical motion than the fiducial run with  $m = 3$ , even though the growth rates are similar ( $\nu/m\Omega_0 = 0.1051$  for  $m = 5$ ). The pressure and density perturbations have noticeable vertical structure, with  $W$  typically increasing away from the midplane. This qualitatively differs from homentropic cases.

### 5.3. Solid Upper Boundary

In the above example, it is perhaps not surprising that entropy perturbations became more negative away from the midplane, because the free boundary condition demands  $|Q| > |W|$  at  $Z = Z_s$ .

We have re-calculated this mode with a solid upper disk boundary (case 3b). Numerically, this condition forces  $W \simeq Q$  at  $Z = Z_s$ . Figure 11 shows the ratio of pressure to density perturbation. The entropy perturbation at intermediate heights is still typically negative, suggesting this to be an intrinsic feature of the instability in these disk models. The flow pattern is very similar to case 3a.

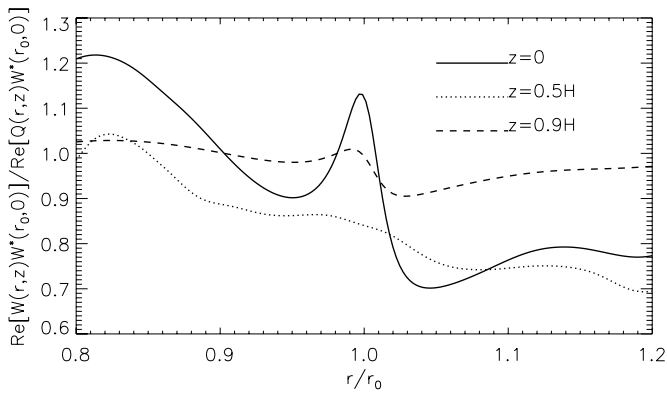


**Figure 11.** Ratio of pressure to density perturbations at  $\phi_0$ , for the nonhomotropic disk with solid upper disk boundaries (case 3b). A ratio above unity implies positive entropy perturbation.

#### 5.4. Effect of $\gamma$ on Vertical Flow

When  $\gamma \neq \Gamma$ , the presence of buoyancy forces is expected to modify the vertical flow associated with the RWI. In Figure 12 we compare the vertical velocity at the vortex core for a range of  $\gamma$ .

As we increase  $\gamma$ , the magnitude of vertical flow increases, with an increasingly complicated  $z$ -dependence. In the homotropic case ( $\gamma = 1.67 = \Gamma$ ),  $\delta v_z$  is essentially linear in  $z$ , consistent with the analytical models of Umurhan (2010). For  $\gamma = 2.5 > \Gamma$ , near the midplane  $\delta v_z$  is still linear in  $z$ , but away from  $z = 0$  the increase in  $\delta v_z$  starts to level off at  $z = 0.3H$  due to the development of meridional vortical motion. The leveling off occurs for both types of upper disk boundary conditions. This results in a “step” in the case of a solid upper boundary (centered about  $z = 0.5H$ ), but for the free upper boundary  $\delta v_z$  increases again at large  $z$ . Since the RWI is a global instability in the vertical direction, vertical boundary conditions can affect the flow throughout the fluid column, though the extent of which depends on the equation of state (Lin 2013; see also Section 6).

Let us examine the different contributions to vertical motion at co-rotation. At  $(r_0, \phi_0)$ , the vertical velocity is roughly

$$\delta v_z \sim -\frac{1}{vH} \underbrace{\left[ \frac{\partial W}{\partial Z} \right]}_{\dagger} + \underbrace{\frac{2nZ\Gamma}{\gamma(1-Z^2)} \left( Q - \frac{\gamma}{\Gamma} W \right)}_{\ddagger}. \quad (33)$$

This equation is obtained from Equation (13) by evaluating it at the co-rotation radius (where  $\bar{\sigma} \simeq -i\nu$ ), and inserting expressions for the pressure length scale for polytropic backgrounds. The first term ( $\dagger$ ) represents pressure forces and is present for all values of  $\gamma$ . For homotropic flow, ( $\dagger$ ) is the only source of vertical motion, and in this case  $W$  decreases with height. The second term ( $\ddagger$ ) is only present if  $\gamma \neq \Gamma$ . Recall the quantity  $Q - \gamma W/\Gamma = \bar{S}$  defined in Section 3.2, where it appeared as a baroclinic source term and we argued  $\bar{S} \leq 0$  at the vortex core (see also Figure 5). Then at the vortex core, ( $\ddagger$ ) contributes positively to  $\delta v_z$  along the vertical direction, but vanishes at endpoints.

In the nonhomotropic example (case 3a,  $\gamma = 2.5$ ) the function  $W$  increases with height at the vortex core (Figure 3), implying ( $\dagger$ ) contributes negatively to  $\delta v_z$ . The contributions from ( $\ddagger$ ) and ( $\dagger$ ) have opposite signs, but the fact that we observe positive vertical velocity shows that ( $\ddagger$ ) is typically larger in magnitude than ( $\dagger$ ). That is, baroclinicity typically outweighs vertical pressure gradients.

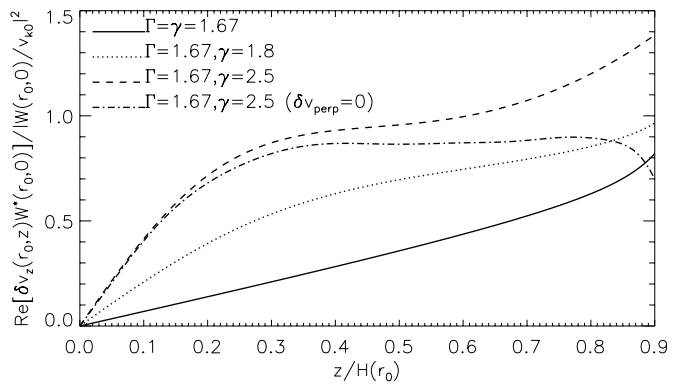


**Figure 12.** Normalized vertical velocities at the vortex core ( $r_0, \phi_0$ ) as function of  $z$ , for several values of  $\gamma$  with fixed  $\Gamma = 1.67$ . The dash-dotted line employed a solid upper disk boundary and other cases use the free boundary condition.

#### 5.4.1. The Role of $N_z^2 \neq 0$

Notice even when  $\gamma$  is only slightly larger than  $\Gamma$ , the vortex core vertical velocity is quite different from the homotropic case (i.e., case 1 with  $\gamma/\Gamma = 1.08$  in Figure 12). To see the role of entropy gradients, or equivalently the effect of non-zero buoyancy frequency, we follow Kato (2001) and make the following approximations. For generality, below we shall not specialize to a polytropic background.

Consider a height at which  $H_s^{-1} \gg L_s^{-1}$ , which is generally true away from the midplane of a thin disk. Furthermore, suppose radial velocities are not much larger than vertical velocities in the region of interest (co-rotation). Then we can neglect the  $\delta v_r$  term in the linearized energy equation, and eliminate  $Q$  between Equations (13) and (15) to obtain

$$\delta v_z \simeq -\frac{1}{v} \left[ \frac{\partial W}{\partial z} + \left( \frac{\partial \ln \rho}{\partial z} - \frac{1}{H_p} \right) W \right] - \frac{N_z^2}{v^2} \delta v_z, \quad (34)$$

which is Kato’s Equation (21) evaluated at co-rotation. Because  $\nu \ll \Omega_0$  for the modes considered and  $N_z \sim \Omega$  away from the midplane, for nonhomotropic flow we have  $N_z^2/\nu^2 \gg 1$  and should expect the balance

$$\delta v_z \sim -\frac{v}{N_z^2} \frac{\partial W}{\partial z} - \underbrace{\frac{v}{N_z^2} \left( \frac{\partial \ln \rho}{\partial z} - \frac{1}{H_p} \right) W}_{-v\rho \left( \frac{\partial p}{\partial z} \right)^{-1} W}, \quad N_z^2 \neq 0 \quad (35)$$

near co-rotation radius. The second term on the right-hand side is just buoyancy (and does not explicitly depend on  $\gamma$ ). This expression should be compared with that for strictly homotropic flow:

$$\delta v_z \sim -\frac{1}{v} \frac{\partial W}{\partial z}, \quad N_z^2 \equiv 0.$$

We see that for  $N_z \equiv 0$ , pressure gradients are entirely responsible for vertical flow, whereas for  $N_z \neq 0$ ,  $\delta v_z$  is result of a combination of pressure and buoyancy forces. The importance of pressure gradients also differ because the coefficients of  $\partial_z W$  are different in each case (by a factor  $\nu^2/N_z^2$ ). Furthermore, the ratio of the first to second term in Equation (35) is approximately

$$\frac{(v/N_z^2) \partial W / \partial z}{\nu \rho |\partial p / \partial z|^{-1} W} \sim \frac{\Omega^2}{N_z^2} \frac{\partial \ln W}{\partial \ln z}. \quad (36)$$

Since  $N_z$  increases with height, far away from the midplane we expect buoyancy forces to dominate in the nonhomentropic case.

We conclude that the origin of vertical motion at co-rotation is qualitatively different between homentropic and nonhomentropic flow (especially away from the midplane), as suggested by numerical results in the previous section.

### 5.5. Fixed $\gamma$ , Variable $\Gamma$

We now fix the adiabatic index to  $\gamma = 1.4$ , as is typical for accretion disk models. Then we require  $n > 2.5$  for axisymmetric stability. With other parameters fixed, increasing  $n$  would decrease the bump in disk thickness and reduce growth rates (L12). To avoid potential numerical issues associated with small  $|\bar{\sigma}|$  at co-rotation, we adopt  $h = 0.2$  for cases 5–8, so that growth rates remain  $O(0.1\Omega_0)$ .

Table 1 shows that by setting  $\gamma \neq \Gamma = 1.33$  (case 6), thereby introducing entropy gradients,  $\langle \theta_m \rangle$  has increased from the homentropic case 5. This is consistent with the trend in cases 0–4.

L12 found that when  $n$  is increased but other parameters fixed, the flow at the vortex core became less 3D. For cases 5–8, we find the average value of  $\theta_m$ , when taken over  $R \in [0.98, 1.02]r_0$ , is 0.46, 0.63, 0.61, and 0.56 for  $n = 2.5, 3.0, 3.5,$  and  $4.0$ , respectively. The flow at  $(r_0, \phi_0)$  in fact becomes more 3D when it is nonhomentropic although  $n$  has increased (case 5  $\rightarrow$  case 6).

The small decrease in the above values of three dimensionality at  $(r_0, \phi_0)$  from  $n = 3.0$  to  $n = 4.0$  is likely related to increased radial flow across  $r_0$  associated with vortical motion in the  $(r, z)$  plane. Cases 6–8 display similar dependence of  $\delta v_z$  on  $z$  as the nonhomentropic example (case 3a, see Figure 12).

## 6. ISOTHERMAL LIMIT

We now examine the limit  $\Gamma \rightarrow 1$ , where the unperturbed disk becomes isothermal, but perturbations are evolved with an adiabatic index  $\gamma = 1.4$ . We consider a nearly isothermal polytropic background and strictly isothermal backgrounds. These cases are treated separately because the equilibrium structures have different functional forms. A comparison between them provides another check on our numerical results.

### 6.1. Large Polytropic Index

We first consider setting  $n = 10$  to produce an almost radially isothermal equilibrium with  $p \propto \rho^{1.1}$ . This allows us to use the numerical code as setup for polytropic equilibria without modification. We also adopt  $A = 2.5$  and  $h = 0.25$  for reasons given in Section 5.5. The relatively large aspect ratio does not violate the thin-disk approximation as large  $n$  implies the density decays rapidly away from the midplane. Also because of this, we set the upper disk boundary at  $Z_s = 0.6$  to avoid very low densities.

For this setup we obtained  $\omega/m\Omega_0 = 0.9883$ ,  $\nu/\Omega_0 = 0.1375$ , and  $\langle \theta_m \rangle = 0.35$ . The top panel of Figure 13 shows the meridional flow at the vortex core. The vortical motion is distinct and more apparent than case 3a, despite the smaller value of  $\gamma/\Gamma$  in the present case. However, apart from this difference, the solution is qualitatively similar to case 3a.

### 6.2. Strictly Isothermal Equilibrium

Modifications to our standard setup are required to treat disk equilibria with  $p = c_{\text{iso}}^2 \rho$  ( $\Gamma \equiv 1$ ), where the constant sound

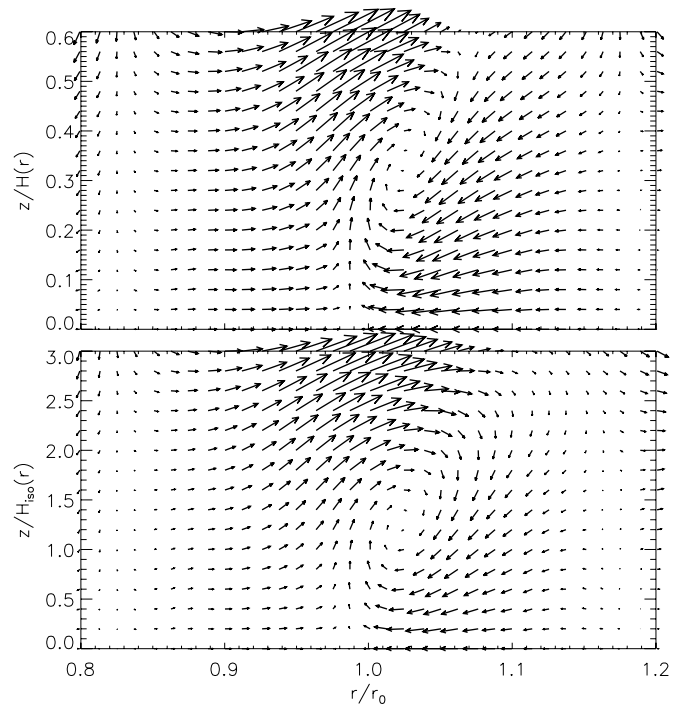


**Figure 13.** Perturbed meridional flow at  $\phi = \phi_0$  for a  $n = 10$  polytropic disk equilibrium (top) and a strictly isothermal equilibrium (bottom).

speed  $c_{\text{iso}} = H_{\text{iso}}\Omega_k$ ,  $H_{\text{iso}} = h_{\text{iso}}r_0(r/r_0)^{3/2}$  is the isothermal scale height, and  $h_{\text{iso}}$  is the characteristic aspect ratio at  $r_0$ . The dimensionless vertical coordinate is now  $Z = z/H_{\text{iso}}$ . The isothermal atmosphere is exponential,  $g(Z) = \exp(-Z^2/2)$ , so there is no surface. In practice we choose a finite vertical domain, i.e.,  $Z = Z_s$  represents a constant number of isothermal scale heights above the midplane.

In the linear code we simply replace expressions for the entropy and pressure length scales by those corresponding to the isothermal disk: the function  $H \rightarrow H_{\text{iso}}$  and  $g(Z)$  becomes the Gaussian above. We choose  $Z_s = 3$  and  $h_{\text{iso}} = 0.05$ , so the isothermal disk has roughly the same temperature as that in the midplane of the large- $n$  polytrope considered above (at  $r_0$ ). In going from the midplane to the upper boundary, the density is also reduced by approximately the same factor for both cases.

We obtain  $\omega/m\Omega_0 = 0.9860$ ,  $\nu/\Omega_0 = 0.1008$ , and  $\langle \theta_m \rangle = 0.39$ . The perturbations plotted in Figure 14 are similar to case 3a, so we expect that these are features of the RWI in nonhomentropic flow, rather than associated with the chosen parameter values. The perturbed meridional flow shown in Figure 13 (bottom panel) is in qualitative agreement with the large- $n$  polytrope. The result is, however, quite different from isothermal linear perturbations, for which Meheut et al. (2012c) found that the vertical velocity appears to have a node at  $r_0$  (see their Figure 3(d) where the vertical velocity changes sign across co-rotation radius, i.e., the fluid column is hydrostatic there). Here, there is clearly vertical motion at co-rotation. Note that both  $\gamma/\Gamma$  and the growth rate are slightly smaller than the nonhomentropic case 3a, but here the vortical motion is more prominent.

Figure 15 shows the vertical velocity at the vortex core as a function of height. The strictly isothermal background (thick solid) has a slightly larger  $\delta v_z$  than the large- $n$  polytrope (thick dashed). This is consistent with previous findings that vertical motions oppose the RWI (Lin 2013), as the former case

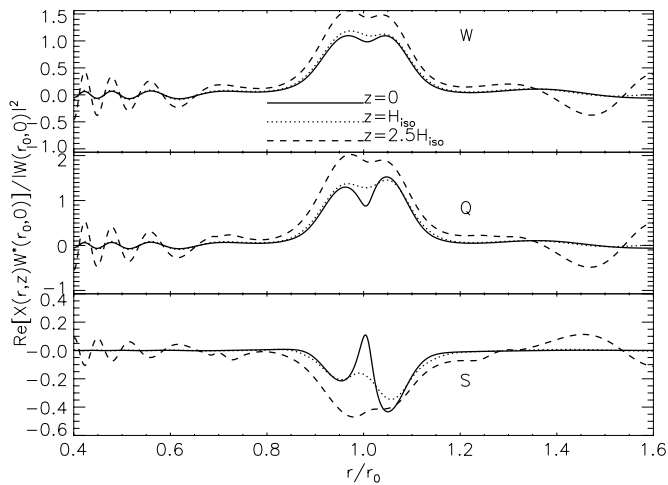


**Figure 14.** Pressure (top,  $W$ ), density (middle,  $Q$ ), and entropy (bottom,  $S$ ) for a globally isothermal background.

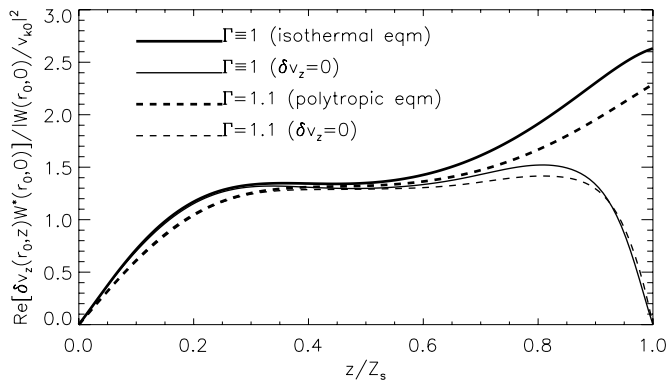


**Figure 15.** Vertical velocity as a function of  $z$  at the vortex core  $(r_0, \phi_0)$ , for the  $n = 10$  polytropic disk equilibrium (dashed) and a strictly isothermal equilibrium (solid) shown in Figure 13, with free upper boundaries (thick lines). Corresponding thin lines impose zero vertical velocity at  $z = Z_s$  (growth rates increased by less than 0.5% from the free boundary condition). Note that changing upper disk boundary conditions only affected the solution near  $z = Z_s$  (cf. Figure 12). This is consistent with Lin (2013), who found the influence of upper disk boundary condition to diminish with increasing polytropic index  $n$ .

has a smaller growth rate than the latter. The thick lines are qualitatively similar to case 3a in Figure 12, but these are not directly comparable because the present case differs in both the background structure and adiabatic index to those in Figure 12.

We illustrate again a correlation between meridional vortical flow and a tilted column of negative vertical vorticity perturbation in Figure 16. The figure is qualitatively similar to that for polytropic backgrounds (case 3a in Figure 9). We find an average tilt of  $1 - \langle \cos \theta \rangle_z = 0.0084 \ll 1$ , so the vorticity column is nearly vertical.

### 6.3. A Nonlinear Simulation

We have also performed global 3D hydrodynamic simulations using the ZEUS-MPfinite-difference code (Hayes et al. 2006). As the focus of this work is the linear problem, we defer a full discussion of these nonlinear simulations to a follow-up paper. Our priority here is to verify the vortical motion in the meridional plane, which appears to be a characteristic feature of the linear RWI solution for nonhomentropic flow.

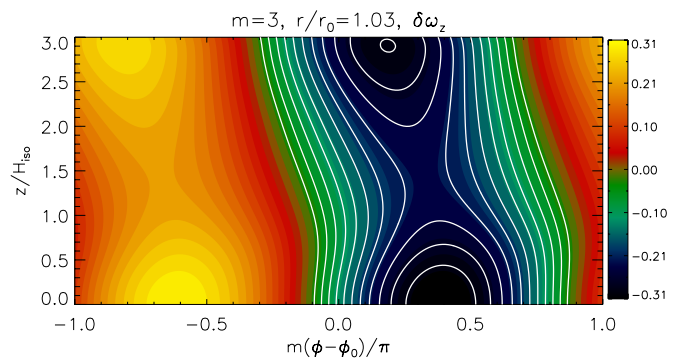


**Figure 16.** Vertical vorticity perturbation,  $\delta\omega_z$ , in the  $(\phi, z)$  plane at  $r = 1.03r_0$  for the strictly isothermal background. Regions of  $\delta\omega \leq 0$  are delineated by white lines. The center of meridional vortical motion identified in Figure 13 occurs at height  $z \sim H_{\text{iso}}$ . The azimuthal range  $\phi - \phi_0 \in [-0.5, 0.5]\pi/m$  corresponds to anti-cyclonic motion about the vortex core. (A plot for  $r = 1.02r_0$  also displays tilted lines of constant  $\delta\omega_z$ , but in that case  $\delta\omega_z > 0$  at  $(\phi_0, H_{\text{iso}})$ .) (A color version of this figure is available in the online journal.)

#### 6.3.1. Setup

We use spherical polar coordinates  $(r_{\text{sph}}, \theta, \phi)$  to describe the disk, taken to be initially strictly isothermal as described above. The computational domain is  $r_{\text{sph}} \in [0.2, 2.0]r_0$ ,  $\theta \in [\theta_{\text{min}}, \pi/2]$ ,  $\phi \in [0, 2\pi]$  and is divided into  $(512, 48, 512)$  zones, with  $\tan(\pi/2 - \theta_{\text{min}}) = 3h_{\text{iso}}$  and  $r_0 = 10$ . The grid is logarithmically spaced in radius and uniformly spaced in the angular coordinates. Boundary conditions are outflow in  $r_{\text{sph}}$ , reflection in  $\theta$ , and periodic in  $\phi$ . Additional damping to meridional velocities near radial boundaries is employed to reduce reflections (de Val-Borro et al. 2007).

After some experimentation, we found it was most convenient to start with a smooth disk. In this case, a surface density  $\Sigma \propto r^{-3/2}$ , and tapered toward the inner boundary (as used in Lin 2012b). We introduce the density bump at  $r = r_0$  via source terms in the mass, momentum, and thermal energy equations, over a timescale of  $10P_0$ , where  $P_0 \equiv 2\pi/\Omega_k(r_0)$ . This reduces numerical transients associated with initialization with a localized bump which has large radial gradients.

We choose the bump amplitude  $A = 1.25$  and isothermal aspect ratio  $h_{\text{iso}} = 0.1$ , as employed by Meheut et al. (2012c) so that we can check our results against theirs. We measure perturbations with respect to azimuthally averaged hydrodynamic quantities at  $t = 10P_0$ .

#### 6.3.2. Results and Comparison to Linear Flow

We focus on the earliest stage of the instability, when perturbation amplitudes are small so comparison with linear calculations can be made. Figure 17 shows the snapshot to be examined, taken at  $t = 23P_0$ . A  $m = 4$  mode has developed from numerical noise. Note the double peak in density perturbation, which is also present in Figure 14. Using the method described in Appendix C, we estimated the  $m = 4$  mode growth rate and frequency to be  $\nu/\Omega_0 \simeq 0.194$  and  $\omega/m\Omega_0 \simeq 0.990$ , in agreement with Meheut et al. (2012c). Although they assumed barotropic perturbations, whereas we simulate adiabatic evolution, our linear calculations indicate that growth rates are largely unaffected by entropy gradients (Table 1).

We have also computed this mode using the linear code as modified for strictly isothermal equilibria, with a solid upper boundary. We obtain the growth rate and mode frequency  $\nu/\Omega_0 = 0.1937$  and  $\omega/m\Omega_0 = 0.9896$ , respectively. This is

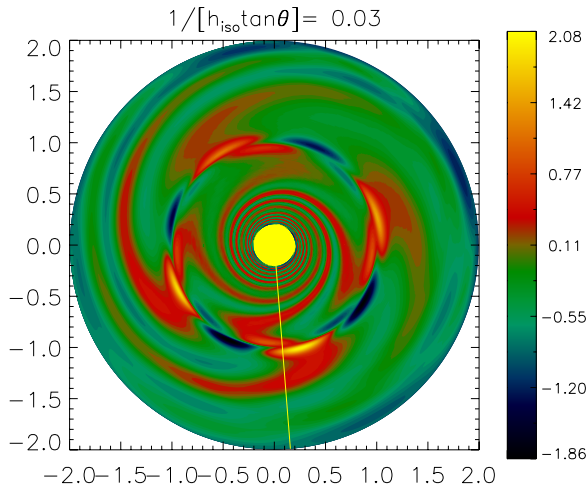


**Figure 17.** Nonlinear hydrodynamic simulation of the RWI in a nonhomotropic 3D disk, initially isothermal but evolved adiabatically. The axes are in units of  $r_0$ . The relative density perturbation near the midplane, scaled by 100, is shown. This quantity is proportional to the  $Q$  used in linear calculations. The smallness of the density perturbation implies that the snapshot corresponds to the linear phase of the instability. The line drawn defines the vortex azimuth  $\phi_0$  in Figures 18 and 19.

(A color version of this figure is available in the online journal.)

close to the nonlinear simulation. Figure 18 compares the density perturbation  $Q$  computed from the hydrodynamic simulation and linear code. They are broadly consistent. The linear code also produces a bias toward the over-density ahead of the vortex core at the midplane. Away from the midplane, the center of the anti-cyclonic motion has shifted downstream. This shows that, even within the linear regime, the vortex has non-negligible vertical structure in the density perturbation (by comparing the two heights in Figure 18).

We compare meridional flows in Figure 19. The perturbed flow is mostly horizontal in both cases. The nonlinear simulation also produces vortical motion in the same sense as the linear calculation. For the ZEUS calculation, we find that the maximum magnitude of the vertical Mach number is  $\sim 1\%$  with a density-weighted average value of 0.15% in the shell  $r_{\text{sph}} \in [0.9, 1.1]r_0$ . The asymmetry of the pressure perturbation about  $r_0$  is captured by the linear code as well. Disagreement toward the upper boundary is not unexpected, since the linear code assumes that the upper boundary is at a constant number of scale heights above the midplane, whereas the spherical grid imposes constant opening angle. However, both plots indicate that  $W$  increases away from the midplane in the region exterior to  $r_0$ .

## 7. SUMMARY AND DISCUSSION

In this paper, we have examined the linear stability of radially structured 3D disks with non-uniform entropy distribution. These calculations may be considered as an extension to the 2D RWI (Li et al. 2000) by adding the vertical dimension, or to the barotropic RWI calculations of L12 by adding an energy equation with a simpler numerical method.

We adopted polytropic disk equilibria so that the magnitude of entropy gradients can be conveniently parameterized by  $\Delta\gamma \equiv \gamma/\Gamma$ , and we focused on the effect of  $\Delta\gamma \geq 1$ . When the background density and velocity field are fixed through  $\Gamma$ , we found that increasing  $\Delta\gamma$  has negligible effect on the instability growth rate. However, the magnitude of pressure and density perturbations increases with height, and the meridional flow

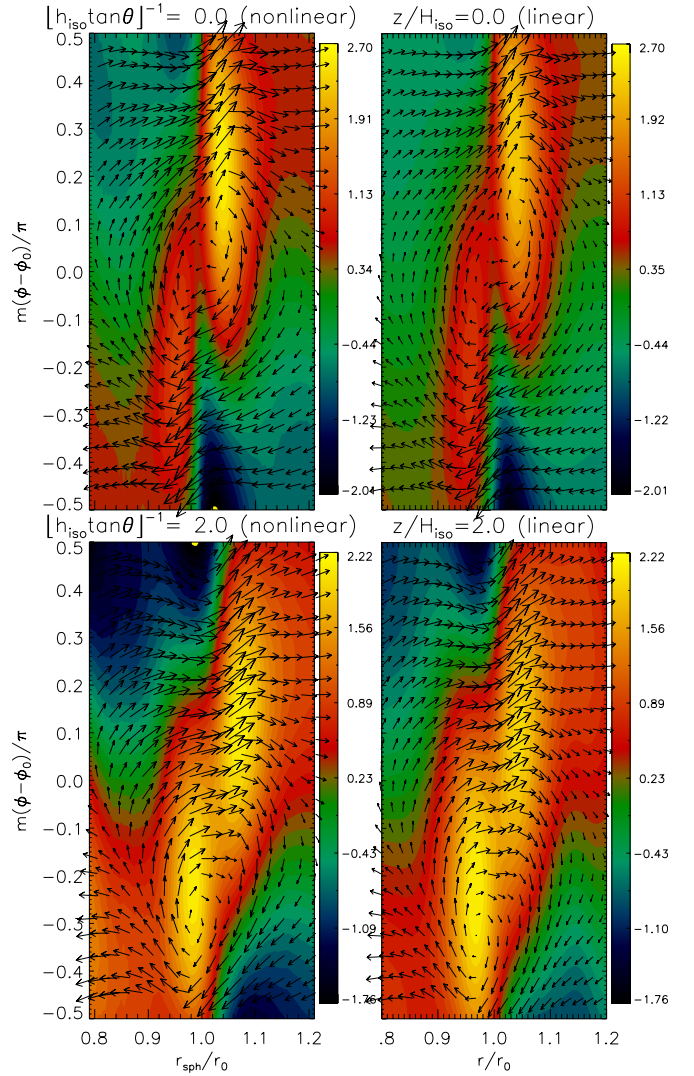


**Figure 18.** Normalized density perturbation,  $Q$ , associated with the RWI computed from a nonlinear hydrodynamic simulation (left) and the linear code (right), at the midplane (top) and at 2 scale heights away from the midplane (bottom). The perturbed velocity field is also shown. The azimuthal wavenumber is  $m = 4$ .

(A color version of this figure is available in the online journal.)

associated with the vortex core is qualitatively changed, with the introduction of meridional vortical motion.

Meridional vortical motion was found to correlate with a small tilt of a fluid column with negative vertical vorticity perturbation. In standard hydrodynamics, vorticity tilting can originate from a contribution of the  $\boldsymbol{\omega} \cdot \nabla \mathbf{v}$  term in the evolution equation of the vorticity independently of the baroclinic source term  $\nabla \rho \times \nabla p$ . However, given the tilt is absent in our homentropic calculations, we associate the tilt with the baroclinic source term, which produces azimuthal vorticity. We also found that the vertical velocity at the vortex core is no longer linear in  $z$ , as for homentropic flow.

In our second set of experiments, we fixed  $\gamma$  and decreased  $\Gamma$ . We found that by making the flow nonhomotropic, the corotation region became *more* 3D, despite the decrease in growth rate. This result is opposite to L12 where lowering  $\Gamma$  made the flow less 3D. This implies that entropy gradients play an important role in the vertical structure of the perturbations.

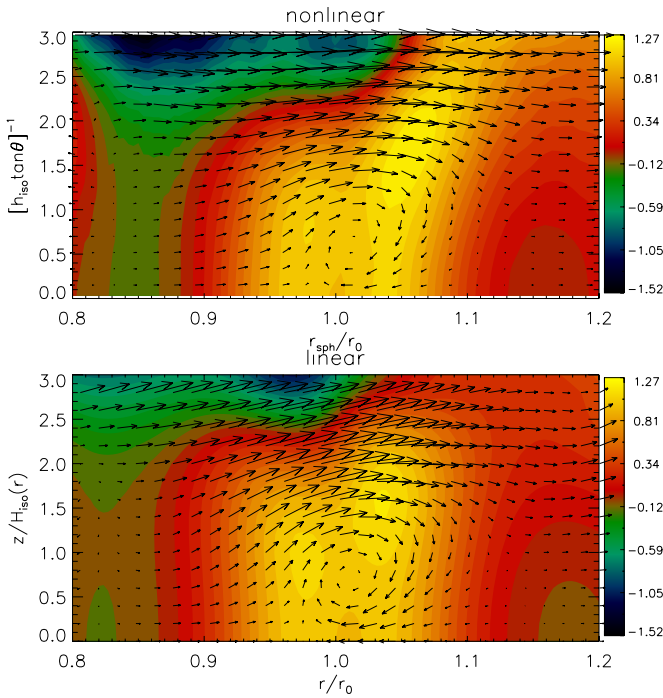


**Figure 19.** Perturbed velocity field projected onto the meridional plane at the vortex azimuth  $\phi_0$ , associated with the RWI calculated from a nonlinear hydrodynamic simulation (top) and the linear code (bottom). The average three dimensionality, as measured by the ratio of vertical to meridional flow speeds,  $\langle \theta_m \rangle$ , is 0.39 and 0.34 in the linear and nonlinear calculations, respectively. A map of the normalized pressure perturbation is also shown. (A color version of this figure is available in the online journal.)

We also considered isothermal equilibria. A linear calculation with  $\Gamma = 1.1$  and one with a strictly isothermal setup ( $\Gamma \equiv 1$ ) were consistent. Both produced prominent meridional vortical motion. In order to verify this feature, we ran a nonlinear simulation of the RWI in an initially isothermal disk, but evolved adiabatically. We indeed identified said vortical motion. Keeping in mind that the setup for linear and nonlinear simulations was not identical (e.g., numerical grid, boundary treatment), similarities between them, such as mode frequency, growth rate, and horizontal flow, are satisfactory.

Vortical motion in the meridional plane thus appears characteristic of the *linear* RWI in nonhomotropic disks. Whether or not this is significant for the vortex evolution can only be answered by detailed long-term nonlinear simulations. If this vortical motion is present in the nonlinear regime then it may prevent dust particles from reaching the disk surface, which occurs for homotropic flow (Meheut et al. 2012b).

However, given that this meridional vortical motion is absent in the homotropic linear solution, it may eventually vanish because of entropy mixing, if no mechanism is present to maintain entropy gradients. For example, the background entropy increases with height but the linear entropy perturbation becomes more negative with height, and its magnitude grows exponentially in time. Indeed, recent 3D fully compressible simulations in nonhomotropic disks show that well into the nonlinear regime, Rossby vortices have columnar structure (Richard & Barge 2013). On the other hand, Meheut et al. (2012c) observed strong meridional vortical motion in their homotropic hydrodynamic simulations; we conclude that they are of nonlinear origin.

In the linear solutions, we often observe perturbation magnitudes increase away from the midplane in nonhomotropic disks<sup>2</sup> (e.g., Figure 19). Then the RWI may not be as robust against vertical boundary conditions as it is to radial boundary conditions. This could pose difficulty for the RWI to develop in dead zones of real protoplanetary disks, which are expected to be confined from above and below by magnetically turbulent layers (Oishi & Mac Low 2009). The vertical boundary condition set by these layers may or may not be compatible with the linear RWI solution.

### 7.1. Caveats and Outlooks

One tradeoff for the simplicity of our numerical method for linear simulations is that a trial eigenfrequency must be guessed. This is not a significant obstacle for the problem at hand because previous RWI studies provide an important guide (Li et al. 2000). Otherwise, zeros of the complex function  $\mathcal{D}(\sigma) = \det U$  need to be located with more rigorous methods (e.g., Kojima 1986; de Val-Borro et al. 2007). We have also exploited previous findings that the PPI and RWI are predominantly 2D (Papaloizou & Pringle 1985; Goldreich et al. 1986; Kojima et al. 1989; Umurhan 2010; Meheut et al. 2012c; Lin 2012a, 2013), which enabled the use of a small number of basis functions. However, there could exist parameter regimes where the RWI has significant vertical structure, rendering our solution method inefficient.

Our conclusions are limited to polytropic backgrounds. While this was convenient for numerical experiments, it is an oversimplification of protoplanetary disks, which are expected to have complicated vertical structure (Terquem 2008). In particular, we found that entropy gradients play a role in the vertical structure of the linear RWI, and even a small entropy gradient can noticeably modify the vertical flow (Section 5.4.1). Thus, a realistic model for entropy evolution is needed.

It would also be of interest to generalize the calculations to *baroclinic* equilibria,<sup>3</sup> for which  $\partial_z \Omega \neq 0$ . This may well be the case when the equilibrium pressure depends on both the density and temperature. Complications from baroclinic instabilities may arise, however (Knobloch & Spruit 1986; Umurhan 2012; Nelson et al. 2012).

We have neglected gas self-gravity in this study. Our models therefore assume that the Toomre parameter is much larger than unity in both the unperturbed *and* perturbed states. However, self-gravity may affect the RWI even when the Toomre parameter is not small (Lovelace & Hohlfield 2013). Previous studies have found that higher  $m$  RWI modes are favored when disk self-gravity is included (Lyra et al. 2008; Lin & Papaloizou 2011). Recent 3D simulations of the RWI in a locally isothermal disk show that vertical self-gravity can noticeably enhance the density perturbation near the midplane, even though the initial disk was considered low mass (Lin 2012b).

In principle, one can express the Poisson integral as a matrix operator and incorporate it into our formalism. The linear problem is further complicated by the need of a numerical solution to the equilibrium equations describing a radially structured, self-gravitating 3D disk (Muto 2011). Such a linear calculation is beyond the scope of this paper, but will be

<sup>2</sup> This reminds us of the off-midplane vortices discovered by Barranco & Marcus (2005) in nonlinear local simulations, but the setup considered in that study is very different from the present work. Nevertheless, in both cases the vertical entropy gradient is stabilizing away from the midplane.

<sup>3</sup> In fact, baroclinic tori were briefly considered by Frank & Robertson (1988).

inevitable for understanding the RWI in 3D self-gravitating disks. Perhaps a simpler starting point, to gain first insight, is direct hydrodynamic simulations including disk gravity. This is indeed the approach we will take in our follow-up paper.

I thank the referee, P. Barge, for suggesting the idea of a tilted vorticity column. I also thank S.-J. Paardekooper for comments on the first version of this paper.

## APPENDIX A PDE COEFFICIENTS

In  $(R, Z)$  coordinates, the coefficients for the PDE pair (Equations (18) and (19)) with dependent variables  $(\tilde{W}, \tilde{Q})$  are

$$\begin{aligned} a_1 &= 1, & b_1 &= -2Z \frac{H'}{H}, & c_1 &= Z^2 \left( \frac{H'}{H} \right)^2 - \frac{D}{\bar{\sigma}^2 H^2}, \\ d_1 &= \left[ \ln \left( \frac{R}{D} \right) \right]', \\ e_1 &= Z \left\{ \left( \frac{H'}{H} \right)^2 - \left( \frac{H'}{H} \right) \left[ \ln \left( \frac{R}{D} \right) \right]' - \left( \frac{H'}{H} \right)' \right\}, \\ f_1 &= \frac{2m\Omega}{R\bar{\sigma}} \left[ \ln \left( \frac{\Omega}{D} \right) \right]' - \frac{m^2}{R^2}, \\ \bar{d}_1 &= -\frac{1}{L_p}, & \bar{e}_1 &= \frac{Z}{L_p} \frac{H'}{H} + \frac{D}{\bar{\sigma}^2 H H_p}, \\ \bar{f}_1 &= \frac{2m\Omega}{L_p R \bar{\sigma}} - \frac{D}{c_s^2} + \frac{D}{\bar{\sigma}^2 H} \frac{\partial H_p^{-1}}{\partial Z} - \frac{1}{L_p} \left[ \ln \left( \frac{R}{D} \right) \right]' \\ &\quad - \frac{\partial L_p^{-1}}{\partial R} + Z \frac{H'}{H} \frac{\partial L_p^{-1}}{\partial Z}, \end{aligned} \quad (\text{A1})$$

and

$$\begin{aligned} d_2 &= \frac{\bar{\sigma}}{L_s D}, & e_2 &= - \left( \frac{Z \bar{\sigma}}{L_s D} \frac{H'}{H} + \frac{1}{\bar{\sigma} H H_s} \right), \\ f_2 &= \frac{2m\Omega}{L_s R D} - \frac{\bar{\sigma}}{c_s^2}, \\ \bar{f}_2 &= \bar{\sigma} \left( \frac{1}{c_s^2} - \frac{1}{D L_s L_p} \right) + \frac{1}{\bar{\sigma} H_p H_s}. \end{aligned} \quad (\text{A2})$$

Note that these coefficients are expressed in terms of pressure, entropy length scales, and the adiabatic sound speed. Although  $H$  has the physical meaning of the polytropic disk thickness, as far as the derivation of these coefficients is concerned, it is simply a function involved in a coordinate transformation. These expressions are therefore valid for any barotropic equilibria.

## APPENDIX B

### NUMERICAL ROUTE TO A MATRIX EQUATION FOR $W$

In Section 3 we arrived at the differential equation  $UW = 0$  by first deriving an equation for  $\tilde{W}$  and then changed the dependent variable to  $W$ . Instead, we can first make the substitution  $\tilde{W} = \rho W$  and  $\tilde{Q} = \rho Q$  in Equations (16) and (17) to obtain the governing equations for  $(W, Q)$ :

$$\begin{aligned} A_1 \frac{\partial^2 W}{\partial R^2} + B_1 \frac{\partial^2 W}{\partial Z \partial R} + C_1 \frac{\partial^2 W}{\partial Z^2} + D_1 \frac{\partial W}{\partial R} + E_1 \frac{\partial W}{\partial Z} + F_1 W \\ + \bar{D}_1 \frac{\partial Q}{\partial R} + \bar{E}_1 \frac{\partial Q}{\partial Z} + \bar{F}_1 Q = 0, \end{aligned} \quad (\text{B1})$$

$$D_2 \frac{\partial W}{\partial R} + E_2 \frac{\partial W}{\partial Z} + F_2 W + \bar{F}_2 Q = 0, \quad (\text{B2})$$

with

$$\begin{aligned} A_1 &= a_1, & B_1 &= b_1, & C_1 &= c_1, & D_1 &= 2a_1 \frac{\rho'_0}{\rho_0} + b_1 \frac{g'}{g} + d_1, \\ E_1 &= b_1 \frac{\rho'_0}{\rho_0} + 2c_1 \frac{g'}{g} + e_1, \\ F_1 &= a_1 \frac{\rho''_0}{\rho_0} + b_1 \frac{\rho'_0}{\rho_0} \frac{g'}{g} + c_1 \frac{g''}{g} + d_1 \frac{\rho'_0}{\rho_0} + e_1 \frac{g'}{g} + f_1, \\ \bar{D}_1 &= \bar{d}_1, & \bar{E}_1 &= \bar{e}_1, & \bar{F}_1 &= \bar{d}_1 \frac{\rho'_0}{\rho_0} + \bar{e}_1 \frac{g'}{g} + \bar{f}_1, \\ D_2 &= d_2, & E_2 &= e_2, & F_2 &= d_2 \frac{\rho'_0}{\rho_0} + e_2 \frac{g'}{g} + f_2, \\ \bar{F}_2 &= \bar{f}_2. \end{aligned} \quad (\text{B3})$$

We recall that the unperturbed density is  $\rho = \rho_0(R)g(Z)$  and primes denote differentiation with respect to the argument. These transformation formulae make no reference to a polytropic background, so they are valid for any equilibrium density field separable in the above form, such as an exponential atmosphere.

When discretized, these equations have the matrix representation

$$U_1 \mathbf{w} + \bar{U}_1 \mathbf{q} = 0, \quad (\text{B4})$$

$$U_2 \mathbf{w} + \bar{U}_2 \mathbf{q} = 0, \quad (\text{B5})$$

where  $\mathbf{q}$  is the vector of pseudo-spectral coefficients for  $Q$ , i.e.,  $Q_i(Z) \equiv Q(R_i, Z) = \sum_{k=1}^{N_z} q_{ki} \psi_k(Z/Z_s)$ . The matrix representation of  $UW = 0$  is then

$$[U_1 - \bar{U}_1 (\bar{U}_2^{-1} U_2)] \mathbf{w} \equiv U \mathbf{w} = \mathbf{0}. \quad (\text{B6})$$

Note that we can divide Equation (B2) by  $\bar{F}_2$  before converting the operators to matrices. Then  $\bar{U}_2$  is a block diagonal matrix consisting only of the Chebyshev polynomials evaluated at vertical grid points. Its inverse can be pre-computed and stored.

In this approach, the user only needs to specify the PDE coefficients defined in Appendix A. The transformed coefficients  $A_1$ – $F_1$  are used to construct the matrix  $U_1$  as described in Lin (2013), and similarly for  $\bar{U}_1$  and  $U_2$ . The final operator,  $U$ , results from matrix multiplication and addition, which standard software can perform.

## APPENDIX C

### ESTIMATING INSTANTANEOUS MODE GROWTH RATES

When dealing with hydrodynamic simulations it may be impractical to frequently output data for explicit computation of time derivatives. This is particularly the case if high spatial resolution simulations are performed. However, we can take advantage of this and exchange time derivatives for spatial derivatives using the fluid equations.

As usual, we denote the Fourier transform with subscript  $m$ , so that

$$\rho_m(r, \theta, t) \equiv \int_0^{2\pi} \rho(r, \theta, \phi, t) \exp(-im\phi) d\phi, \quad (\text{C1})$$

where we have adopted spherical coordinates, so here  $r$  is the spherical radius. Taking a time derivative and using the continuity equation gives

$$\frac{\partial \rho_m}{\partial t} = - \int_0^{2\pi} \nabla \cdot (\rho \mathbf{v}) \exp(-im\phi) d\phi. \quad (\text{C2})$$

Writing this out in full, applying the usual rule for Fourier transforms to the azimuthal contribution to the divergence, we obtain

$$-\frac{\partial \rho_m}{\partial t} = \frac{1}{r^2} \frac{\partial}{\partial r} [r^2 (\rho v_r)_m] + \frac{1}{r \sin \theta} \frac{\partial}{\partial \theta} [\sin \theta (\rho v_\theta)_m] + \frac{im}{r \sin \theta} (\rho v_\phi)_m. \quad (\text{C3})$$

We can therefore just use the Fourier transform of momentum densities to calculate time derivatives of a Fourier mode. The complex frequency  $\sigma$  is defined through  $\partial_t \rho_m = i\sigma \rho_m$ , from which we extract the mode frequency  $\omega$  and growth rate  $\nu$ . These are spatially dependent when obtained from simulation data using the above procedure. So we average  $\omega$  and  $\nu$  over the  $\theta$  domain and around co-rotation  $r \in [0.8, 1.2]r_0$ . This gives an estimate of the instantaneous growth rate and pattern speed of a mode with azimuthal wavenumber  $m$  at time  $t$ .

## REFERENCES

- Armitage, P. J. 2011, *ARA&A*, 49, 195  
 Barge, P., & Sommeria, J. 1995, *A&A*, 295, L1  
 Barranco, J. A., & Marcus, P. S. 2005, *ApJ*, 623, 1157  
 Crespe, E., Gonzalez, J.-F., & Arena, S. E. 2011, in Proc. Annual Meeting of the French Society of Astronomy and Astrophysics, SF2A-2011, ed. G. Alecian et al. (<http://sf2a.eu/proceedings/2011>)  
 de Val-Borro, M., Artymowicz, P., D'Angelo, G., & Peplinski, A. 2007, *A&A*, 471, 1043  
 Frank, J., & Robertson, J. A. 1988, *MNRAS*, 232, 1  
 Gammie, C. F. 1996, *ApJ*, 457, 355  
 Goldreich, P., Goodman, J., & Narayan, R. 1986, *MNRAS*, 221, 339  
 Hayes, J. C., Norman, M. L., Fiedler, R. A., et al. 2006, *ApJS*, 165, 188  
 Inaba, S., & Barge, P. 2006, *ApJ*, 649, 415  
 Kato, S. 2001, *PASJ*, 53, 1  
 Klahr, H. 2004, *ApJ*, 606, 1070  
 Knobloch, E., & Spruit, H. C. 1986, *A&A*, 166, 359  
 Kojima, Y. 1986, *PThPh*, 75, 251  
 Kojima, Y. 1989, *MNRAS*, 236, 589  
 Kojima, Y., Miyama, S. M., & Kubotani, H. 1989, *MNRAS*, 238, 753  
 Li, H., Colgate, S. A., Wendroff, B., & Liska, R. 2001, *ApJ*, 551, 874  
 Li, H., Finn, J. M., Lovelace, R. V. E., & Colgate, S. A. 2000, *ApJ*, 533, 1023  
 Li, H., Lubow, S. H., Li, S., & Lin, D. N. C. 2009, *ApJL*, 690, L52  
 Lin, D. N. C., & Papaloizou, J. 1986, *ApJ*, 309, 846  
 Lin, M.-K. 2012a, *ApJ*, 754, 21  
 Lin, M.-K. 2012b, *MNRAS*, 426, 3211  
 Lin, M.-K. 2013, *MNRAS*, 428, 190  
 Lin, M.-K., & Papaloizou, J. C. B. 2010, *MNRAS*, 405, 1473  
 Lin, M.-K., & Papaloizou, J. C. B. 2011, *MNRAS*, 415, 1426  
 Lovelace, R. V. E., & Hohlfield, R. G. 2013, *MNRAS*, 429, 529  
 Lovelace, R. V. E., Li, H., Colgate, S. A., & Nelson, A. F. 1999, *ApJ*, 513, 805  
 Lyra, W., Johansen, A., Klahr, H., & Piskunov, N. 2008, *A&A*, 491, L41  
 Lyra, W., Johansen, A., Zsom, A., Klahr, H., & Piskunov, N. 2009, *A&A*, 497, 869  
 Lyra, W., & Mac Low, M.-M. 2012, *ApJ*, 756, 62  
 Meheut, H., Casse, F., Varniere, P., & Tagger, M. 2010, *A&A*, 516, A31  
 Meheut, H., Keppens, R., Casse, F., & Benz, W. 2012a, *A&A*, 542, A9  
 Meheut, H., Meliani, Z., Varniere, P., & Benz, W. 2012b, *A&A*, 545, A134  
 Meheut, H., Yu, C., & Lai, D. 2012c, *MNRAS*, 422, 2399  
 Muto, T. 2011, *ApJ*, 739, 10  
 Narayan, R., Goldreich, P., & Goodman, J. 1987, *MNRAS*, 228, 1  
 Nelson, R. P., Gressel, O., & Umurhan, O. M. 2012, arXiv:1209.2753  
 Oishi, J. S., & Mac Low, M.-M. 2009, *ApJ*, 704, 1239  
 Paardekooper, S.-J., Baruteau, C., Crida, A., & Kley, W. 2010, *MNRAS*, 401, 1950  
 Papaloizou, J. C. B., & Pringle, J. E. 1984, *MNRAS*, 208, 721  
 Papaloizou, J. C. B., & Pringle, J. E. 1985, *MNRAS*, 213, 799  
 Papaloizou, J. C. B., & Pringle, J. E. 1987, *MNRAS*, 225, 267  
 Richard, S., & Barge, P. 2013, in EPJ Web of Conferences, Instabilities and Structures in Proto-planetary Disks, in press  
 Tanaka, H., Takeuchi, T., & Ward, W. R. 2002, *ApJ*, 565, 1257  
 Tassoul, J.-L. 2000, *Stellar Rotation* (Cambridge: Cambridge Univ. Press)  
 Terquem, C. E. J. M. L. J. 2008, *ApJ*, 689, 532  
 Umurhan, O. M. 2010, *A&A*, 521, A25  
 Umurhan, O. M. 2012, *A&A*, 543, A124  
 Varnière, P., & Tagger, M. 2006, *A&A*, 446, L13  
 Yu, C., Li, H., Li, S., Lubow, S. H., & Lin, D. N. C. 2010, *ApJ*, 712, 198  
 Zhang, H., & Lai, D. 2006, *MNRAS*, 368, 917  
 Zhuravlev, V. V., & Shakura, N. I. 2007, *AstL*, 33, 740